Computational efficient process simulation of geometrically complex parts in metal additive manufacturing

Yang, Y.; Ji, Y.; Möller, M.; Ayas, C.

DOI
10.1016/j.ijheatmasstransfer.2025.127059

Publication date
2025

Document Version
Final published version

Published in
International Journal of Heat and Mass Transfer

International Journal of Heat and Mass Transfer 248 (2025) 127059

Contents lists available at ScienceDirect

International Journal of Heat and Mass Transfer

journal homepage: www.elsevier.com/locate/hmt

Computational efficient process simulation of geometrically complex parts in metal additive manufacturing

Y. Yang [a,*], Y. Ji [b], M. Möller [b], C. Ayas [a]

[a] Computational Design and Mechanics Group, Department of Precision and Microsystems Engineering, Faculty of Mechanical Engineering, Mekelweg 2, Delft, 2628 CD, The Netherlands

[b] Delft Institute of Applied Mathematics, Delft University of Technology, Mekelweg 4, Delft, 2628 CD, The Netherlands

ARTICLE INFO

Keywords:
Laser powder bed fusion
Thermal process modeling/simulation
Image source

ABSTRACT

Part-scale thermal process simulations play an important role in improving the part quality of the Laser Powder Bed Fusion (LPBF) process. The semi-analytical simulation method relies on the superposition of analytical fields to represent laser-induced heat sources in a semi-infinite space and a complementary temperature field to enforce boundary conditions. So far, boundary conditions have been imposed by analytical image fields for straight boundaries and numerically for non-straight boundaries. The latter requires considerable refinement on the spatial discretization, at least near the boundaries, and compromises the computational efficiency of the simulations. In this paper, we derive a closed-form solution for the image fields that can accurately enforce the boundary conditions for non-straight boundaries. A geometrically complex part boundary is represented by B-splines, and with the aid of an offset method and reparameterization, the positions of the image sources are determined. The image field's closed-form expression is then found using the boundary's local curvature calculated from the local tangent lines. Numerical examples on different levels of complexity revealed that the net heat lost along an adiabatic boundary vanishes when the novel image source solutions are used, and the thermal evolution of complex parts can be accurately predicted with high computational efficiency. Simulations involving multiple lasers can also be performed with no extra computational cost.

1. Introduction

Laser Powder Bed Fusion (LPBF) is a metal additive manufacturing process that builds parts ranging from a few millimeters to centimeters. In the LPBF, one or multiple lasers serve as localized and instantaneous heat sources, melting and fusing the powder to construct 3D parts layer by layer. Several thermal processes occur during this process, including heat absorption by the metal powder from the laser(s), phase changes between solid, liquid, and even gas states, heat conduction, radiation, and convection. To begin with, the metal powder partially absorbs the laser energy, triggering a phase change from solid to liquid as the temperature reaches the melting point. Subsequently, when the lasers move away, rapid solidification occurs as the molten metal cools. Heat conduction is critical throughout this process in conveying heat to the build platform, which serves as a heat sink. Moreover, the heat transfer between the already solidified part and the surrounding metal powder is insignificant, as the thermal conductivity of the metal powder is approximately 1% of the solid part [1]. Additionally, radiation transfers part of the energy to the surrounding environment, especially in the high-temperature melt pool zone. Convection also occurs between the part and the inert gas in the chamber. These thermal processes collectively influence the microstructural evolution, residual stress, and distortion, thereby, the part quality and mechanical properties [2].

Optimal process parameters (e.g., laser power and scanning velocity) are essential to avoid defects, warping, residual stress, and poor surface finish while ensuring dimensional accuracy and mechanical performance. However, determining the optimal process parameters through experiments alone is challenging and costly. In addition to laser power and scanning velocity, the laser scanning strategy (or path) plays a crucial role in thermal evolution. Currently, advanced 3D metal printers are equipped with multiple lasers, operating simultaneously to enhance the speed of the printing process. Consequently, the complexity of laser scanning further increases since more freedom is allowed in scanning with multiple lasers involved. Therefore, optimizing the laser scan vectors along with laser power and velocity becomes even more burdensome. Thermal

* Corresponding author.
E-mail addresses: Y.Yang-13@tudelft.nl (Y. Yang), y.ji-1@tudelft.nl (Y. Ji), m.moller@tudelft.nl (M. Möller), C.Ayas@tudelft.nl (C. Ayas).

https://doi.org/10.1016/j.ijheatmasstransfer.2025.127059
Received 12 December 2024; Received in revised form 20 March 2025; Accepted 1 April 2025
Available online 8 May 2025

simulations of the LPBF process serve as an invaluable tool, providing insights for optimizing process parameters and scanning strategies. Such models help predict thermal behavior, allowing for better control over the process to achieve desired part quality and mechanical properties.

Various numerical methods have been employed to compute the part-scale thermal history of the printing process. Finite Element Method (FEM) is widely adopted for solving the heat conduction process during metal additive manufacturing [3–6]. Sarkar [7] presented a comprehensive review of the state-of-the-art FEM applications in the LPBF process. The use of FEM in this context dates back to welding simulations, as LPBF and welding share many common features [8]. Lindgren [9–11] gave an overview of FEM applications in modeling and simulating welding processes, in which the elements representing filler material addition are activated during simulation, named as element birth and death method. Similarly, the element birth and death method simulates the growing domain nature of the LPBF process. This method can be further categorized into two types: the quiet element method and the inactive element method. In the quiet element method, elements corresponding to layers that are not yet realized are disabled by scaling down their thermal conductivity in the global conductivity matrix [12]. In contrast, in the inactive element method, these elements are not assembled into the global conductivity matrix [13]. Lu et al. [14] adopted the inactive element method to predict the residual stress and distortion of Ti–6Al–4V thin wall structures. Chiumenti et al. [15,16] improved this method by adding a new kind of activated elements that correspond to the new activated domain in the current moment. As a result, there are two different types of elements in the computational domain, one corresponding to the previously activated elements and one corresponding to the newly activated elements. The newly activated elements are activated at the material's melting temperature to avoid spurious thermal stresses from interacting with active elements. However, a finite element (FE) mesh must capture steep temperature gradients around the laser. Since lasers scan the entire part and thus interact with the whole simulation domain, albeit in different instances, spatial discretization is bound by the characteristic length scale, i.e. the laser size spot radius [13,17]. For instance, Roberts et al. [13] adopted an element length of half of the laser source radius. Thus, these approaches can lead to an excessive number of elements in FEM and result in compromised computational efficiency.

Adaptive mesh refinement has been proposed to refine the mesh within laser interaction areas and dynamically coarsen it in regions far from the current laser spot positions. This method attracted significant attention due to its ability to reduce computational costs by reducing the number of degrees of freedom. Both h-refinement (refining the mesh size h) and hp-refinement (refining the mesh size and increasing the polynomial degrees of the trial/test space p) have been utilized [18–22]. Most simulations utilize a layer-wise (static) remeshing scheme, where the mesh is progressively refined after each layer deposition or after the deposition of several layers. Consequently, the mesh remains uniformly fine along the entire scanning path within the uppermost layers [18]. Li et al. [23] proposed an Octree mesh coarsening strategy for 3D printing thin wall structures. In this strategy, the mesh is dynamically coarsened towards the bottom layers, and the length of the finite elements doubles for each coarsening.

In contrast, the scan-wise (dynamic) remeshing scheme refines the mesh in the vicinity of the laser spot to capture steep temperature gradients following the laser motion. A relatively coarse mesh is used in regions away from the laser spot where the local temperature is more uniform [24,25]. Compared to the layer-wise remeshing scheme, the scan-wise remeshing further decreases the number of degrees of freedom but requires the mesh to be frequently updated according to the laser positions during single-layer scanning. However, a computationally efficient way of adopting an analytical temperature field is proposed to remedy the need for the local mesh refinement [26].

These approaches rely on analytical solutions of heat equation in a semi-infinite space to represent the instantaneous laser exposure [26–30], either in the form of a Riemann sum of individual closed-form expressions of point heat sources generated incrementally [26,31], or as a line source field through integrating the temperature contribution of infinitesimal point sources along a line [28–30]. Since the analytical field effectively captures the steep temperature gradients near the laser spot, there is no need for a moving fine mesh to capture these gradients numerically, significantly reducing computational complexity. Extensive research has been conducted using the analytical approach, exploring various aspects such as temperature history under different scanning strategies [32,33], melt pool geometry [31,34,35], and temperature-dependent thermal conductivity [29,36]. Nevertheless, there is not always a closed-form temperature expression for arbitrary shapes of laser sources and complex laser scanning paths. Thus, Forslund et al. [37] introduced a method to integrate each segment of a laser scan path under a moving Gaussian heat source. Depending on the parameters of the heat source, the required quadrature orders are different to achieve the desired level of accuracy. Stump et al. [38] also conducted a study to improve the numerical integration of the point-source temperature field using Gaussian quadrature. This scheme discretizes a continuous line scan into a series of segments with adaptive time integration length. It demonstrates higher computational efficiency and more accurate temperature predictions than just using a simple Riemann sum of closed-form temperature fields from individual point sources [38]. The limited accuracy of the analytical temperature field arises from the assumption of a semi-infinite space, while the additive manufactured parts are finite. Therefore, boundary conditions of the finite part are not satisfied.

In the semi-analytical method, the temperature field is described by the superposition of the above-described analytical temperature field and a complementary numerical field to enforce the boundary conditions [26]. Within this method, adiabatic boundary conditions are usually assumed since the thermal conductivity of the metal powder is approximately 1% of the solid part [1,28,39], and the heat loss through convection and radiation on the boundary surface is relatively small compared to heat conduction within the solid part [13,26,40]. However, Ning et al. [27] applied the semi-analytical method using negative static point heat sources on boundary surfaces and an equivalent power method to account for heat loss due to convection and radiation. In this paper, we assume the boundary conditions to be adiabatic and use FEM as the numerical method of choice to calculate the complementary numerical field in the semi-analytical method [28,39]. Since the closed-form temperature field of the point sources captures steep temperature gradients around the laser spot, FE mesh is decoupled from the characteristic length scale of temperature gradients and hence can be much coarser. However, the FE mesh in the vicinity of the boundary must be sufficiently fine to resolve and correct for the outgoing heat flux due to the laser scanning near the boundary. Therefore, using FEM to apply the boundary conditions will still lead to excessive computational cost.

In our previous work, we incorporated analytical image sources to alleviate this computational burden to enforce the adiabatic boundary conditions by reflecting the point heat sources across the part boundaries [26]. This method allows a significantly coarser mesh for the entire domain and immensely reduces the computational cost. However, only straight boundaries can be considered with this method [26]. This is because only along straight boundaries, heat flux contributions from image and regular sources entirely cancel each other. For complex boundaries, the distances between image sources and boundary points differ from those of regular sources at most locations along the boundaries. Consequently, the adiabatic boundary conditions cannot be satisfied solely through image sources. Steuben et al. [29] proposed a method to achieve zero-flux boundary conditions using an image line source across part curve boundaries. This method provides an analytical description of the temperature field by combining a line source and its corresponding image with no numerical correction field. The intensity of the image line source is adjusted by a modulation factor that accounts for the relative speed of the regular (i.e., the scanning velocity) and image sources. However, whether the modulated

image source can achieve adiabatic boundary conditions everywhere on the local boundary is still unknown. Veldman et al. [41] proposed an imaging method to achieve zero-flux boundary conditions analytically. Nevertheless, the image part is not a solution to the homogeneous heat equation and is thus not related to any physical heat source term.

This paper aims to fill this knowledge gap by focusing on image sources for geometrically complex parts with curved boundaries to enforce adiabatic boundary conditions. The main contributions in this paper are as follows:

- A method of modulating the power of image sources is proposed to realize the approximate adiabatic boundary conditions, particularly for complex boundaries represented by B-splines. By offsetting B-spline curves, we can easily generate the regular point source positions in the domain and corresponding image source positions out of the domain. The modulation factor is derived and approximated to a simple closed form based on local curvatures from the B-spline parameter space.
- By employing the analytical temperature fields of regular sources and modulated image sources, the requirement for a fine mesh along part boundaries to impose adiabatic boundary conditions becomes unnecessary. The modulated image sources lead to a much smoother correction field, which requires fewer degrees of freedom to capture numerically. In this way, we achieve higher computational efficiency while ensuring accurate temperature predictions and accounting for the laser scan vectors for parts with complex geometries.

The remainder of the paper is organized as follows: in Section 2, we introduce the semi-analytical method based on the discrete point sources. The position and power modulation of image sources for curved boundaries are described to achieve the desired adiabatic boundary conditions. The closed-form expression for the modulation factor is derived by balancing the flux through the curved boundaries due to regular and image sources. In Section 3, we first compare the heat loss rate on part boundaries in a single-source scenario. Next, we examine a case where a laser scans next to an arc boundary. Temperature histories and computational efficiencies are evaluated and compared using only regular sources, regular and non-modulated image sources, and regular and modulated image sources. Finally, the proposed method is extended to dual laser scanning and demonstrated in geometrically complex cases, and the key contributions of the study are reiterated.

2. Methodology

Consider the LPBF process of a 3D part with an arbitrary shape. Printing a new layer starts with recoating a layer of metal powder on the already printed body V. Therefore, the body V is submerged in the powder bed as shown in Fig. 1a. The surface ∂V of the body V comprises: the top surface ∂V_{top}, the lateral surface ∂V_{lat}, and the bottom surface ∂V_{bot}, such that $\partial V = \partial V_{\text{top}} \cup \partial V_{\text{lat}} \cup \partial V_{\text{bot}}$, as shown in Fig. 1b. The top surface ∂V_{top} and the lateral surface ∂V_{lat} are covered with powder, while the bottom surface ∂V_{bot} is fused to the build platform. The origin of the coordinate system is shown in Fig. 1a, and the build orientation is along the positive x_3-axis. When the metal powder partially absorbs the emitted laser beam, the temperature field of the body evolves, governed by the heat equation

$$\rho c_p \frac{\partial T}{\partial t} = \nabla \cdot (k \nabla T) + Q \quad \text{in } V, \tag{1}$$

where T is the temperature field, ρ the mass density, c_p the heat capacity, k the thermal conductivity and Q the applied thermal load due to the laser. When we neglect the temperature dependence of ρ, c_p and k, Eq. (1) simplifies to its linear form

$$\frac{\partial T}{\partial t} = \alpha \nabla^2 T + \frac{Q}{\rho c_p} \quad \text{in } V, \tag{2}$$

where $\alpha = k/\rho c_p$ is the thermal diffusivity.

To quantify Q, the continuous laser scan is discretized into N regular point sources shown in Fig. 1a. The point source I is activated at time $\tilde{t}^{(I)}$ and the subsequent point source $I+1$ is activated at time $\tilde{t}^{(I+1)} = \tilde{t}^{(I)} + \Delta t$, where $I = 1, \dots, N-1$, and Δt is the temporal step size for time integration. Consequently, the distance between source I and $I+1$ is $v\Delta t$, where v is the laser scanning velocity. Since a series of consecutively activated sources represent the continuous laser scan. The accuracy of this representation depends on the number of point sources dictated by the temporal step size Δt. The convergence study in our previous paper shows that the temporal step size is related to the thermal conductivity and should be smaller than 5×10^{-5} s [26]. In all numerical examples that include a line scanning in Section 3, we use a relatively conservative $\Delta t = 1 \times 10^{-5}$ s to discretize continuous laser scans. When all laser scanning vectors of the current layer are completed, a new layer of metal powder is recoated.

To obtain the temperature distribution inside the domain V, we solve a boundary value problem (BVP) governed by Eq. (2) with boundary conditions on ∂V and the initial condition $T(x_i, 0) = T_c$ at $t = 0$, where T_c is the build platform temperature assumed to be constant. As explained above, the thermal conductivity of the metal powder is approximately 1% of the solid part [1]. Thus, the heat transfer between the solid part and the metal powder is neglected. Moreover, we disregard the heat loss through convection and radiation because their effect is relatively small compared to heat conduction within the solid part [13,26,40]. Consequently, adiabatic boundary conditions are applied on ∂V_{lat} and ∂V_{top} as

$$\frac{\partial T}{\partial x_i} n_i = 0 \quad \text{on } \partial V_{\text{lat}} \cup \partial V_{\text{top}}, \tag{3}$$

where n_i denotes the components of the surface unit outward normal vector, and the boundary condition for the bottom surface ∂V_{bot} is

$$T = T_c \quad \text{on } \partial V_{\text{bot}}. \tag{4}$$

Eqs. (2)–(4) do not explicitly consider the powder-liquid–solid state changes. The effects of heat absorption and release during state changes are neglected since the amount of heat absorbed during melting is subsequently released during solidification within short time intervals [26].

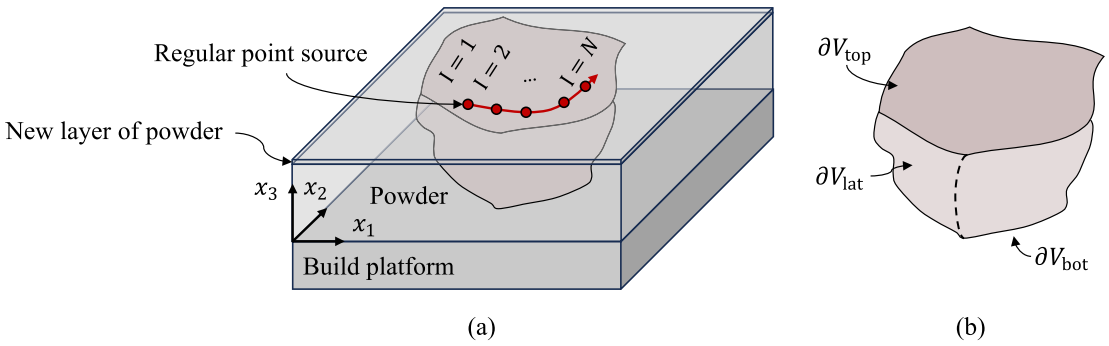

Fig. 1. Schematic illustration of (a) the body V submerged into the powder bed, ∂V_{bot} fused to the build platform. The laser is emitted on the top layer, scanning along an arbitrary trajectory shown with the red curve. (b) the body V with its surface ∂V consisting of ∂V_{top}, ∂V_{lat} and ∂V_{bot}. (For interpretation of the references to colour in this figure legend, the reader is referred to the web version of this article.)

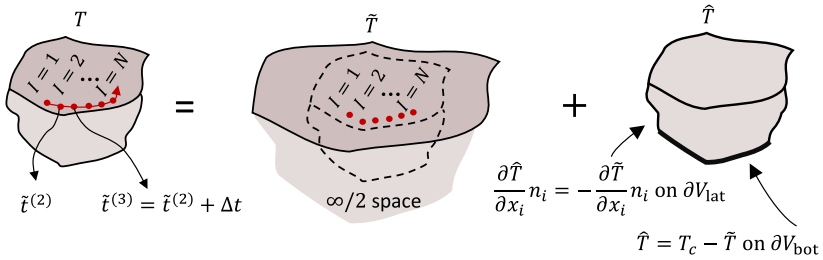

Fig. 2. A continuous line scan is discretized into a series of point sources. The total temperature field is obtained by the superposition of the temperature field due to point sources in semi-infinite space and the complementary temperature field to enforce boundary conditions.

2.1. Semi-analytical method for part-scale thermal simulation

Consider a laser scanning line as shown in Fig. 2. The continuous laser scan is discretized into N point sources on ∂V_{top}. The point sources are activated sequentially in accordance with their respective activation times. For this process, to solve the boundary value problem (BVP) outlined in Eqs. (2)–(4), the total temperature field T is expressed as the superposition of two terms [26] shown in Fig. 2 as

$$T = \tilde{T} + \hat{T}, \tag{5}$$

where $\tilde{T}$ is the analytical temperature field due to currently activated K out of total N sources. The temperature field $\tilde{T}$ is then given as

$$\tilde{T}(x_i, t) = \sum_{I=1}^{K} \tilde{T}^{(I)}(x_i, t), \quad \tilde{t}^{(K)} \le t \text{ and } K \le N, \tag{6}$$

where

$$\tilde{T}^{(I)}(x_i, t) = \frac{QA}{4\rho c_p (\pi\alpha(t - \tilde{\tau}^{(I)}))^{3/2}} \exp\left(\frac{-(R^{(I)})^2}{4\alpha(t - \tilde{\tau}^{(I)})}\right) \tag{7}$$

is the analytical solution of a point source in a half-infinite space, with the origin plane coinciding with ∂V_{top}. The distance between the point source location $\tilde{x}_i^{(I)}$ and the point of interest x_i is $R^{(I)}$. The input energy associated with each point source is $Q = P\Delta t$, where P is the laser power. A is the laser absorptivity fraction of metal powder. To account for the finite radius of the laser source and to avoid singularities at $t = \tilde{t}^{(I)}$, a time shift $\tilde{\tau}^{(I)} = \tilde{t}^{(I)} - r^2/8\alpha$ is applied in Eq. (7), where r denotes the laser spot radius. The time shift corresponds to diffusion distance in the material [26]. We note in passing, the temperature field of a point source with the time shift becomes the temperature field of a 3D Gaussian source with the laser spot radius r and a shape factor 2. This is demonstrated in Appendix A.

To impose the desired boundary conditions on ∂V, an additional field $\hat{T}$ is introduced to correct the analytically obtained field $\tilde{T}$ such that $\tilde{T} + \hat{T}$ meets the desired boundary conditions. The $\hat{T}$ field is governed by

$$\frac{\partial \hat{T}}{\partial t} = \alpha \nabla^2 \hat{T} \quad \text{in } V, \tag{8}$$

with boundary conditions derived from Eqs. (3) and (4) as

$$\frac{\partial \hat{T}}{\partial x_i} n_i = -\frac{\partial \tilde{T}}{\partial x_i} n_i \quad \text{on } \partial V_{lat}, \tag{9}$$

$$\hat{T} = T_c - \tilde{T} \quad \text{on } \partial V_{bot}, \tag{10}$$

and the initial condition at $t = 0$ is $\hat{T}(x_i, 0) = T(x_i, 0) - \tilde{T}(x_i, 0)$, and $T(x_i, 0) = T_c$. In fact, since $\tilde{T}(x_i, 0) = 0$, the initial condition at $t = 0$ becomes $\hat{T}(x_i, 0) = T_c$. It should be noted that no numerical correction is required on ∂V_{top} since the adiabatic top surface coincides with the origin of semi-infinite space. The adiabatic boundary conditions on the top surface of the part are automatically satisfied and built-in Eq. (7). In principle,

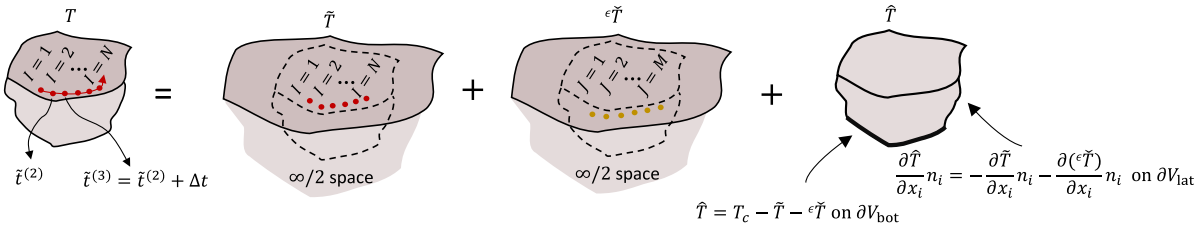

Fig. 3. The total temperature field represented as the superposition of the temperature field of regular sources in semi-infinite space, the temperature field of image sources in semi-infinite space, and the complementary temperature field to apply boundary conditions. (For interpretation of the references to colour in this figure legend, the reader is referred to the web version of this article.)

the $\hat{T}$ is a smooth field since it contains no point sources. Consequently, the temperature field $\hat{T}$ can be solved with a standard numerical method FEM with a mesh size no longer dictated by the laser spot radius.

Nevertheless, when the point source I is located in the vicinity of ∂V_{lat}, the temperature gradients associated with $\tilde{T}^{(I)}$ at the part boundary ∂V_{lat} notably impairs the smoothness of $\hat{T}$, necessitating fine spatial discretization for accurate numerical solutions. Therefore, the FE mesh close to the lateral boundaries ∂V_{lat} needs to be refined in the order of laser spot radius r to resolve the temperature field associated with the laser beam [28]. To maintain computational efficiency without requiring such mesh refinement, we introduce image sources to assist in enforcing the boundary conditions.

Consider the temperature field in response to a laser scan vector, as illustrated in Fig. 2. The field is now represented as the superposition of three distinct temperature components, as shown in Fig. 3. The analytical field $\tilde{T}$ in Eq. (6) is due to regular point sources activated sequentially at each time step, marked by red dots. The corresponding image sources outside the body V are activated simultaneously to offset the high heat flux at the lateral boundary ∂V_{lat} due to nearby regular sources. The temperature decomposition in Eq. (5) is thus extended to include three components associated with the activated regular sources, rewritten as the superposition of three terms,

$$T = \tilde{T} + {}^{\epsilon}\check{T} + \hat{T}, \tag{11}$$

where

$${}^{\epsilon}\check{T}(x_i, t) = \sum_{J=1}^{K} \epsilon^{(J)} \check{T}^{(J)}(x_i, t), \quad \check{t}^{(K)} < t \text{ and } K \le M, \tag{12}$$

and

$$\check{T}^{(J)}(x_i, t) = \frac{QA}{4\rho c_p (\pi\alpha(t - \check{\tau}^{(J)}))^{3/2}} \exp\left(\frac{(R^{(J)})^2}{4\alpha(t - \check{\tau}^{(J)})}\right). \tag{13}$$

Note that, $\check{T}^{(J)}$ in Eq. (13) is similar to $\tilde{T}^{(I)}$ in Eq. (7), and also a closed-form solution in a semi-infinite space bounded by the top surface ∂V_{top}. Here, $R^{(J)}$ is the distance between the point of interest x_i and the image source location $\check{x}_i^{(J)}$.[1] The activation time of each image source J is $\check{\tau}^{(J)}$, and at time t, K out of M image sources are activated. Note that the total number of image sources is much less than regular sources, as an image source is only created for a regular source sufficiently close to the lateral boundary. The critical distance d_c of a regular source to ∂V_{lat} is proposed to be less than or equal to $15r$ to induce an image source. Recall that when a regular source is away from a boundary, the temperature field due to the regular source is smooth on the boundary. The complementary field $\hat{T}$ described on a coarse FE mesh is thus sufficient to enforce the boundary condition at a desired level of accuracy. Therefore, there is no need to incorporate an image source when a regular source is away from a boundary. The proposed modulation factor $\epsilon^{(J)}$ scales the power of image source J, and approximates the net heat flux from a pair of regular and image sources across the associated complex boundary to zero.

Similarly, for the decomposition in Eq. (11) and the BVP given in Eqs. (2)–(4), the $\hat{T}$ field remains governed by Eq. (2) but with boundary conditions

$$\frac{\partial \hat{T}}{\partial x_i} n_i = -\frac{\partial \tilde{T}}{\partial x_i} n_i - \frac{\partial ({}^{\epsilon}\check{T})}{\partial x_i} n_i \quad \text{on } \partial V_{\text{lat}}, \tag{14}$$

$$\hat{T} = T_c - \tilde{T} - {}^{\epsilon}\check{T} \quad \text{on } \partial V_{\text{bot}}, \tag{15}$$

and the initial condition at $t = 0$ is $\hat{T}(x_i, 0) = T(x_i, 0) - \tilde{T}(x_i, 0) - {}^{\epsilon}\check{T}(x_i, 0)$. Since $T(x_i, 0) = T_c$ and $\tilde{T}(x_i, 0) = \check{T}(x_i, 0) = 0$, the initial condition at $t = 0$ becomes $\hat{T}(x_i, 0) = T_c$. By and large, the image sources neutralize the heat flux emanating from regular sources close to the lateral boundaries. Consequently, the $\hat{T}$ field remains smooth and can be resolved with a coarse FE mesh. However, image source compensations for straight and curved boundaries are different. In Fig. 4a, the exact adiabatic boundary conditions are achieved for the straight boundary ∂V_1 when the image source J and the regular source I are symmetrically located on opposite sides of ∂V_1, and the image source is outside the solid domain, with a modulation factor $\epsilon^{(J)} = 1$. Thus, the power of the regular source I is equal to that of the image source J. It can be easily observed that the heat flux components along the surface normal direction generated by the regular and image sources are equal in magnitude and opposite in sign everywhere along the straight boundary ∂V_1. In Fig. 4b, the regular source I is positioned at a distance d from the semicircular boundary. Its corresponding image source J is placed symmetrically across the boundary at the same distance d. At point p, where the semicircular boundary intersects the line connecting the regular and image sources, the distances from p to both sources are equal, and the net heat flux along the surface normal vanishes. However, this is not the case for any other point on the semicircular boundary. As a result, zero heat flux condition is not enforced for the vast majority of points on the part boundary ∂V_2. Nevertheless, approximate adiabatic boundary conditions can be achieved on average along boundary segments by introducing a modulation factor $\epsilon^{(J)}$. The value of $\epsilon^{(J)}$ for each image source J is determined by its distance from the boundary and the local curvature of the boundary.

[1] The details of identifying the positions of image sources across a complex boundary are discussed in Section 2.3.

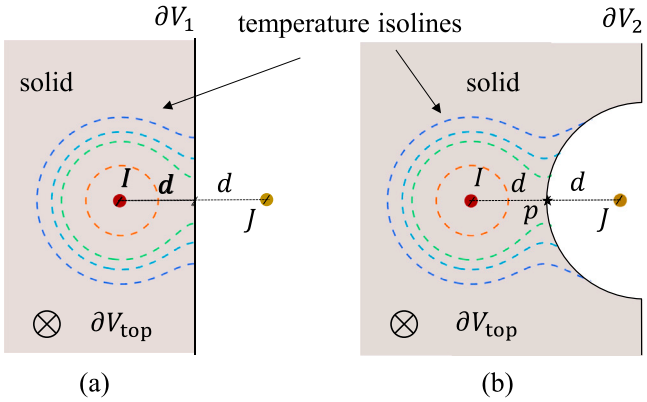

Fig. 4. Schematic illustration temperature isolines of field of $\tilde{T}^{(I)}+\epsilon^{(J)}\tilde{T}^{(J)}$. The regular source I and J are on the top surface of the semi-infinite space. (a) The adiabatic boundary ∂V_1 divides the semi-infinite space into two parts, and the part to the left of the adiabatic boundary ∂V_1 is solid. The distances between the boundary and both regular source I and image source J are d, and the adiabatic boundary conditions on ∂V_1 are satisfied. The modulation factor is $\epsilon^{(J)}=1$. (b) The adiabatic boundary ∂V_2 divides the semi-infinite space into two parts, and the part to the left of the adiabatic boundary ∂V_2 is solid. The adiabatic boundary conditions are not enforced with the regular source I and image source J with the modulation factor $\epsilon^{(J)}=1$.

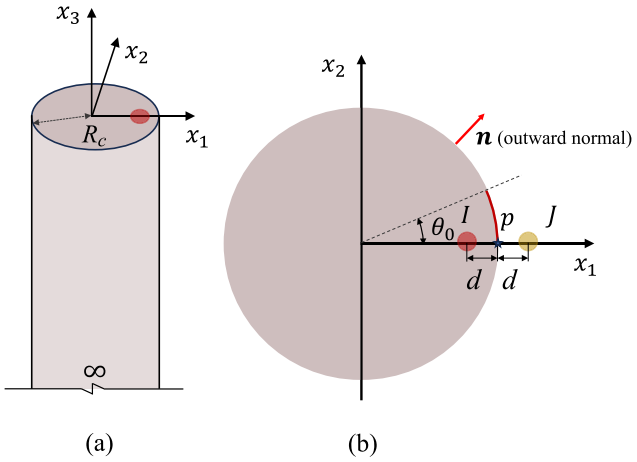

Fig. 5. Single source model for modulation factor calculation. (a) A point heat source on the top surface of an infinitely long cylinder with radius R_c. (b) Plane $x_3=\tilde{x}_3^{(I)}$ contains the image source for the point heat source and line integration arc (red solid line) for calculating local energy conservation. θ_0 is the corresponding central angle of the arc. The distance of the regular source and image source to the boundary is d. (For interpretation of the references to colour in this figure legend, the reader is referred to the web version of this article.)

2.2. Modulation factor derivation on an infinitely long cylinder

It remains to derive a general expression for the modulation factor. Consider an infinitely long solid cylinder with the radius R_c shown in Fig. 5 where the top surface of the cylinder is at the origin of the semi-infinite space. A regular point source I is located on the top surface of the cylinder at $\tilde{x}_i^{(I)}$, and the distance between the regular source I and the adiabatic boundary is d. The corresponding image source J is placed out of the solid cylinder domain to neutralize the heat flux on the adiabatic boundary due to the point source I. Using Eq. (7) and direct differentiation, the component of temperature gradient of the regular point source I is

$$\frac{\partial\tilde{T}^{(I)}(x_i,t)}{\partial x_i}=\frac{QA}{4\rho C_p(\pi\alpha(t-\tilde{\tau}^{(I)}))^{3/2}}\exp\left(\frac{-(R^{(I)})^2}{4\alpha(t-\tilde{\tau}^{(I)})}\right)\frac{2\tilde{x}_i^{(I)}-2x_i}{4\alpha(t-\tilde{\tau}^{(I)})}. \tag{16}$$

For a point with coordinates x_i on the lateral surface of the cylinder, the outward normal is

$$[n_1,n_2,n_3]^\top=[\frac{x_1}{R_c},\frac{x_2}{R_c},0]^\top. \tag{17}$$

Now, consider the plane $x_3=\tilde{x}_3^{(I)}$ illustrated on Fig. 5b. The heat flux across the surface in the outward direction at a point on the circular boundary due to the regular point source I is

$$\begin{aligned}\tilde{q}^{(I)}(x_i,t)&=-k\frac{\partial\tilde{T}^{(I)}(x_i,t)}{\partial x_i}n_i\\&=\frac{\nu}{(t-\tilde{\tau}^{(I)})^{3/2}}\exp\left(\frac{-(x_1-\tilde{x}_1^{(I)})^2-(x_2-\tilde{x}_2^{(I)})^2}{4\alpha(t-\tilde{\tau}^{(I)})}\right)\left(\frac{-\tilde{x}_1^{(I)}x_1+(x_1)^2-\tilde{x}_2^{(I)}x_2+(x_2)^2}{2\alpha(t-\tilde{\tau}^{(I)})}\right)\frac{1}{R_c},\end{aligned} \tag{18}$$

where ν is

$$\nu = \frac{kQA}{4\rho c_p(\pi\alpha)^{3/2}}. \tag{19}$$

It can be observed that ν depends on the laser power and thermal material properties, which are constant in this paper. The dot product performed in Eq. (18) projects the heat flux vector along the outward normal direction. In fact, Eq. (18) can be interpreted as the heat loss rate at the point x_i on the boundary. The heat flux along the surface normal direction increases as the point source location gets closer to the cylindrical boundary (i.e. decreasing d shown in Fig. 5b). Due to the symmetry of the solid cylinder along the x_1-axis and the regular source also being positioned on the x_1-axis, we investigate the red arc boundary segment above the x_1-axis in Fig. 5. An image source J, as shown with a yellow circle in Fig. 5b, is placed outside the solid domain to neutralize the heat flux on the red arc emitted from the regular point source, and the image source J is also on the plane $x_3 = \tilde{x}_3^{(I)}$. Similarly, the heat loss rate due to the image source J on the circular boundary is

$$\begin{aligned}\breve{q}^{(J)}(x_i,t) &= -\epsilon^{(J)} k \frac{\partial \breve{T}^{(J)}(x_i,t)}{\partial x_i} n_i \\ &= \frac{\epsilon^{(J)}\nu}{(t-\breve{\tau}^{(J)})^{3/2}} \exp\left(\frac{-(x_1-\breve{x}_1^{(J)})^2-(x_2-\breve{x}_2^{(J)})^2}{4\alpha(t-\breve{\tau}^{(J)})}\right)\left(\frac{-x_1^{(J)}x_1+(x_1)^2-x_2^{(J)}x_2+(x_2)^2}{2\alpha(t-\breve{\tau}^{(J)})}\right)\frac{1}{R_c},\end{aligned} \tag{20}$$

where the power of the image source is modulated by $\epsilon^{(J)}$. In the simplest case of image sources for straight adiabatic boundaries [42], $\epsilon^{(J)} = 1$, where the power of regular and image sources are equal for an infinitely large radius of curvature R_c. When the radius of curvature R_c is finite, the distance between the image source and point p in Fig. 5 is equal to the distance between the regular source and point p. However, for any other point on the boundary segment, these distances differ—the distance from the image source to the point is different from the regular source to the point. As a result, adiabatic boundary conditions on the boundary segment cannot be exactly achieved using an image source. However, the regular source I only heats a limited area around the source, and most of the heat loss due to source I happens from the boundary segments near the source location. Assuming that the heat loss due to the source I during a given time interval along the red arc surface in Fig. 5 is $\tilde{\Phi}^{(I)}$, and the corresponding heat loss due to the source J is $\breve{\Phi}^{(J)}$. The average adiabatic boundary condition on the red arc is acquired through

$$\tilde{\Phi}^{(I)} = \breve{\Phi}^{(J)}. \tag{21}$$

By solving Eq. (21), with simplifications and an approximation given in Appendix B, the $\epsilon^{(J)}$ becomes

$$\epsilon^{(J)} = \frac{4R_c + d}{4R_c - d}\sqrt{\frac{R_c + d}{R_c - d}}. \tag{22}$$

Through the modulation factor $\epsilon^{(J)}$, the net heat loss is negligible on the boundary segment close to the sources I and J. It should be noted that Eq. (22) is based on a convex solid part surface shown in Fig. 5. For a concave solid part surface, $\epsilon^{(J)}$ becomes

$$\epsilon^{(J)} = \frac{4R_c - d}{4R_c + d}\sqrt{\frac{R_c - d}{R_c + d}}. \tag{23}$$

Moreover, it can be verified that, when $R_c \to \infty$, both Eqs. (22) and (23) yield $\epsilon^{(J)} = 1$. That corresponds to no modulation needed for image sources on straight boundaries. It remains to find the image source locations and compute the modulation factor for the more general case with complex boundaries.

2.3. Image source generation for complex part geometry constructed by B-splines

An inherent advantage of the LPBF process is its remarkable capacity to manufacture geometrically intricate structures with high precision. This section introduces the B-spline curve generation method for representing the geometrically complex part boundaries. Then, we derive an offset method to express the contour line scan path along part boundaries parametrically. Next, a reparameterization method is introduced to discretize the continuous contour line scan path into uniformly spaced point sources. After the discretization, as shown in Fig. 6, the corresponding image source positions for each regular point source are determined based on the local tangent line of the curve. The separation distances between the regular and image point source to the curve tangent line are d, shown in Fig. 6. Modulation factors are then computed using Eqs. (22) and (23), taking into account the local curve curvature.

2.3.1. B-spline curves

Consider a knot vector, which is a non-decreasing sequence of real numbers, denoted as

$$\Xi = \left[\underbrace{0,0,\ldots,0}_{p+1},\xi_{p+1},\xi_{p+2},\ldots,\xi_n,\underbrace{1,1,\ldots,1}_{p+1}\right].$$

Given this knot vector Ξ, the ith B-spline basis function of degree p can be generated utilizing the Cox-de Boor recursion formula [43]

$$N_{i,p}(\xi) = \frac{\xi-\xi_i}{\xi_{i+p}-\xi_i}N_{i,p-1}(\xi) + \frac{\xi_{i+p+1}-\xi}{\xi_{i+p+1}-\xi_{i+1}}N_{i+1,p-1}(\xi), \tag{24}$$

starting from

$$N_{i,0}(\xi) = \begin{cases} 1, & \text{if } \xi \in [\xi_i, \xi_{i+1}), \\ 0, & \text{otherwise,} \end{cases}$$

where any ratios of the form $0/0$ are conventionally defined as zero.

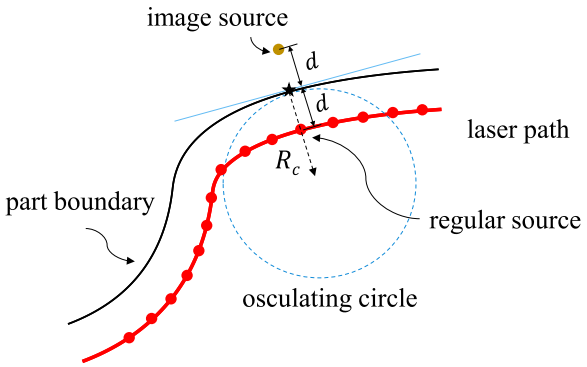

Fig. 6. Laser scan path generation by offsetting part geometry boundaries and corresponding image source position.

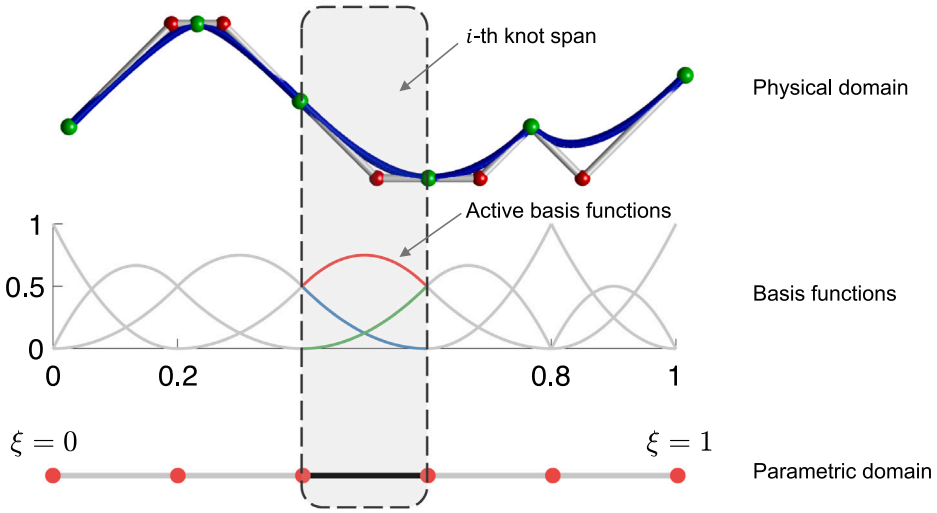

Fig. 7. A quadratic ($p = 2$) B-spline curve constructed using B-spline basis functions defined over an open knot vector $\Xi = [0, 0, 0, 0.2, 0.4, 0.6, 0.8, 0.8, 1, 1, 1]$.

A Non-Uniform Rational B-Splines (NURBS) curve of degree p can be then characterized as a vector-valued function

$$C(\xi) = \sum_{i=0}^{n} \mathbf{P}_i R_{i,p}(\xi), \ \ \xi \in \hat{\Omega} = [0, 1], \tag{25}$$

where $\mathbf{P}_i \in \mathbb{R}^3$ are the control point coordinates that govern the shape and position of the curve, $\hat{\Omega}$ is referred to as the parametric domain, and $R_{i,p}(\xi)$ are the rational B-spline basis functions defined by

$$R_{i,p}(\xi) = \frac{N_{i,p}(\xi)\omega_i}{\sum_{i=0}^{n} N_{i,p}(\xi)\omega_i}, \ \ i = 0, 1, \ldots, n, \tag{26}$$

where ω_i denotes the weight associated with the control point $\mathbf{P}_i$. Fig. 7 presents quadratic B-spline basis functions constructed over the knot vector $\Xi = [0, 0, 0, 0.2, 0.4, 0.6, 0.8, 0.8, \ 1, 1, 1]$ along with a B-spline curve defined over these basis functions.

2.3.2. Offset curve

As laser scans along the part boundary, the laser beam is usually kept at a constant distance from the part boundaries. A straightforward approach to parametrically generate the contour laser scan path is offsetting the boundary curves with a constant distance d. However, directly computing offsets for B-spline curves is complicated. To this end, we introduce an alternative method that transforms the initial curve to create an offset counterpart uniformly distanced from the part geometry by a specified distance. Firstly, we compute the offset of a series of discretized point sources on the part geometry.

After discretizing the part geometry into a series of points $(x_1^{(I)}, x_2^{(I)})$, $I = 1, 2, \ldots, N$, we subsequently offset these points by a specified distance d to define the laser path, as shown in Fig. 6. For each point $(x_1^{(I)}, x_2^{(I)})$, we compute the corresponding tangent vector $\boldsymbol{v}^{(I)}$ by taking the derivative of the B-spline curve, formally expressed as

$$\boldsymbol{v}^{(I)} = C(\xi^{(I)}) = \sum_{i=0}^{n} \mathbf{P}_i \frac{\partial R_{i,p}(\xi^{(I)})}{\partial \xi_i}, \quad I = 1, 2, \ldots, N, \tag{27}$$

where $\xi^{(I)}$ denotes the parameter associated with the point $(x_1^{(I)}, x_2^{(I)})$. We then determine the normal vector $[n_1^{(I)}, n_2^{(I)}]^\top$ by rotating $\boldsymbol{v}^{(I)}$ by 90 degrees. The offset vector is computed by scaling the normal vector with the desired offset distance d, expressed as $[dn_1^{(I)}, dn_2^{(I)}]^\top$. This calculation

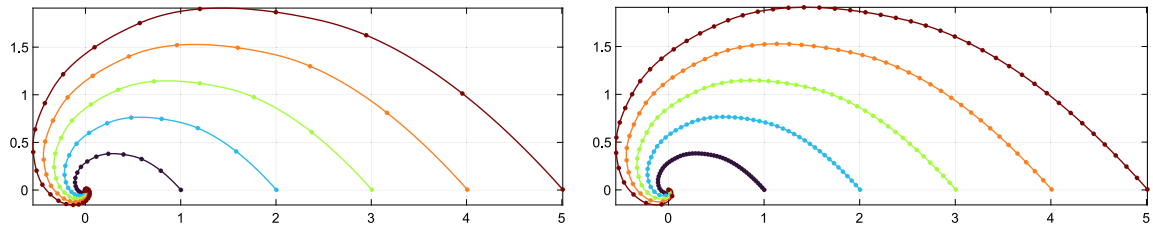

Fig. 8. Logarithmic spiral curve before (a) and after (b) arc-length reparameterization, with $m = 50$ control coefficients and polynomial degree $p = 2$.

Table 1
Ti–6Al–4V thermal properties:

Conductivity	Heat capacity	Density
42 (W/mK)	990 (J/kgK)	4420 (kg/m^3)

forms the basis for determining the position of the laser path, given by

$$\begin{aligned} \bar{x}_1^{(I)} &= x_1^{(I)} + d n_1^{(I)}, \\ \bar{x}_2^{(I)} &= x_2^{(I)} + d n_2^{(I)}. \end{aligned} \tag{28}$$

These coordinates $(\bar{x}_1^{(I)}, \bar{x}_2^{(I)})$ represent the points along the laser path, effectively creating the desired offset from the original curve. However, it should be noted that the distance is not constant for adjacent points $(\bar{x}_1^{(I)}, \bar{x}_2^{(I)})$ along the laser path. With the laser path coordinates now determined, we revert these points to a B-spline curve configuration $\boldsymbol{C}$ by applying a least-squares fitting with chord-length parameterization, as described in Section 9.4.1 of [43].

2.3.3. Arc-length reparameterization

After getting the laser scan path by offsetting and fitting a series of points on the geometry boundaries, we need to discretize the continuous laser scan path into evenly distributed discrete point sources as shown in Figs. 3 and 6, which means the distance between two successive point sources to be constant. A common approach is arc-length parameterization, characterized by the equitable distribution of arc lengths over corresponding curve segments. The formulation process is detailed in Appendix C. Fig. 8 showcases the input curves alongside their respective reparameterized versions, derived using the proposed approximate arc-length approach. This transformation significantly improves the uniformity of the resulting curves compared to the original. With a reparameterized curve $\boldsymbol{C}(\xi(\hat{\xi}))$, equidistant points can be easily obtained through uniform sampling. To be more specific, to achieve a sampling with a constant distance d_s between successive points, one would uniformly sample $\lfloor L/d_s \rfloor$ points along the reparameterized curve, where $\lfloor\ \rfloor$ denotes the floor function, rounding down to the nearest integer, L the total length of the curve.

3. Numerical examples and comparison of results

This section will investigate several part geometries, from simple to more complex ones. Initially, we examine the heat loss rate distribution, i.e. heat flux in the surface outward direction, along a curved boundary, in the presence of a regular point heat source and its image counterpart. Then, we consider a contour laser scan and compare temperature histories and heat loss rate distributions under three temperature decomposition methods. The first approach is decomposing the total temperature field using Eq. (5), where the analytical temperature field consists of contributions due to regular sources only. In the second and third methods, the total temperature field is decomposed using Eq. (11), where the analytical temperature fields image sources $\breve{T}$ are accounted for without and with modulating the image source power, respectively. Subsequently, we extend our proposed method of using modulated image sources to a dual laser scanning scenario. Lastly, we demonstrate our method in simulating more intricate parts enclosed by boundaries of varying curvatures.

3.1. A single point source on a curved boundary

In this section, we compare heat loss rate distribution q, of a regular source Eq. (18) and its image part Eq. (20), on the simple part shown in Fig. 9. The part features a curved boundary with a fixed radius of curvature $R_c = 2$ mm. A laser exposure time 1×10^{-5} s, a laser power $P = 82.5$ W, a spot radius $r = 20\,\mu$m and an energy absorptivity fraction 0.77 are assumed. The non-modulated image source J has the same power and spot radius. The regular point source is located on the top surface of the part as shown in Fig. 9. Since the image source is reflected symmetrically in the radial direction of the arc boundary, the arc center, regular source, and image source are on a line. The shortest distance between the image source and the arc boundary is $100\,\mu$m, the same as that of the regular source. The angular coordinate θ is defined with respect to the x_2-axis. The lateral surfaces of the part are considered to be adiabatic, and the bottom surface is assumed to be kept at a constant temperature. We consider the thermal properties representative of Ti–6Al–4V throughout the paper given in Table 1.

The numerical complementary field $\hat{T}$ is omitted in this section only to study the heat loss rate distribution of the regular and image sources. Therefore, we calculate the heat loss rate q distribution along the arc boundary on the top surface for the regular source ($\tilde{q}$), the non-modulated image source ($\breve{q}$), the modulated image source ($^{\epsilon}\breve{q}$), and pairs of the regular and the non-modulated image ($\tilde{q}+\breve{q}$) and the regular and the modulated image sources ($\tilde{q} + {}^{\epsilon}\breve{q}$). From Eq. (23), the modulation factor is calculated as $\epsilon^{(J)} = 0.86$, which scales down the heat loss rate distribution of the image source. The heat loss rate distribution at the boundary is plotted as a function of θ in Fig. 10. The two sources are generated at $t = 0$, and the activation time of the sources is calculated with a time shift $\tau = 0 - r^2/8\alpha$, as discussed in Section 2.1. The heat loss rate distribution is plotted

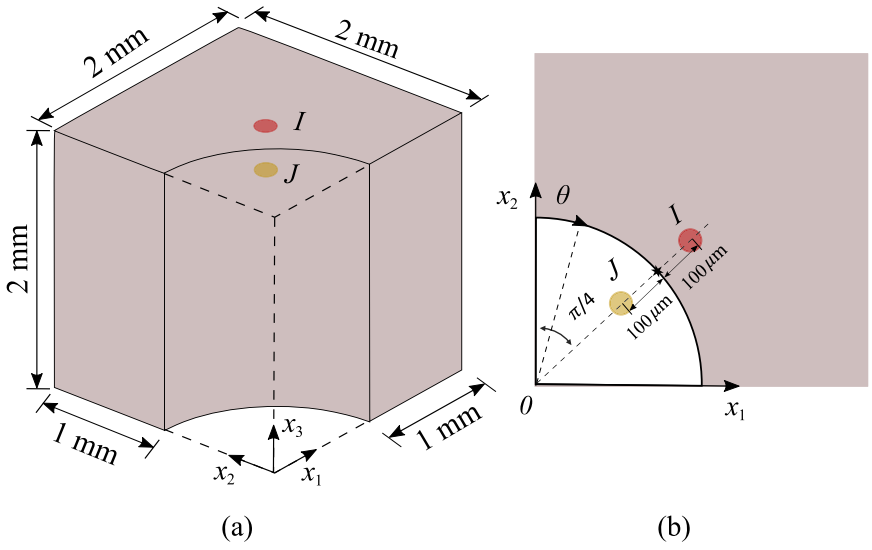

Fig. 9. (a) A regular point source (red) is located near the curved surface on a $2\,\text{mm} \times 2\,\text{mm} \times 2\,\text{mm}$ cube where a cylinder with a radius $R_c = 1\,\text{mm}$ is carved out from its corner, and the corresponding image source (yellow). (b) Top view of the part. The regular source, the image source, and the arc center are on a line. The shortest distances from the image and the regular source to the arc are $100\,\mu\text{m}$. The image and regular sources are located at $\theta = \pi/4$ with respect to the x_2 axis. (For interpretation of the references to colour in this figure legend, the reader is referred to the web version of this article.)

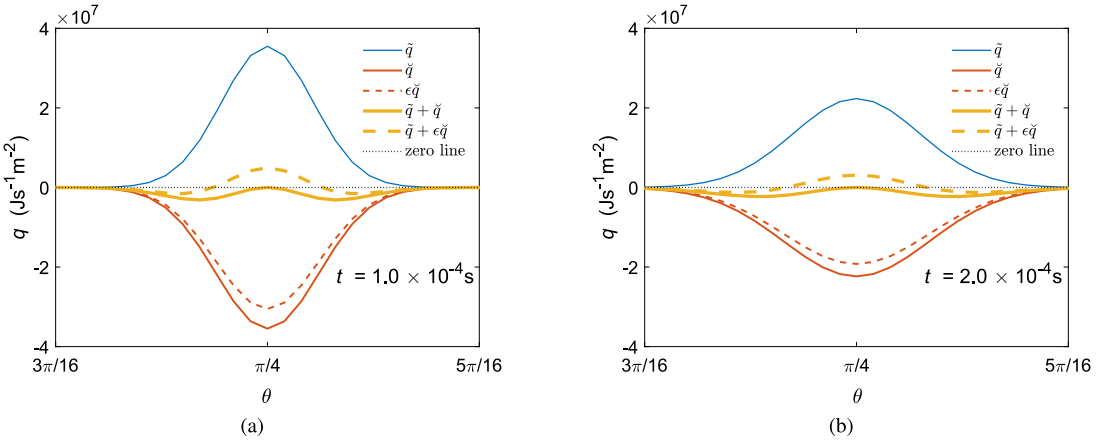

Fig. 10. Heat loss rate q distribution along the arc boundary of five cases at (a) $t = 1.0 \times 10^{-4}$ s and (b) $t = 2.0 \times 10^{-4}$ s. Heat loss rate distribution of the regular source $\tilde{q}$, heat loss rate distribution of the non-modulated image source $\breve{q}$, heat loss rate distribution of the modulated image source ${}^{\epsilon}\breve{q}$, heat loss rate distribution of the regular and non-modulated image sources $\tilde{q}+\breve{q}$, and heat loss rate distribution of the regular and modulated image sources $\tilde{q}+{}^{\epsilon}\breve{q}$. Both the image and regular sources are located at $\theta = \pi/4$ with respect to the x_2 axis. (For interpretation of the references to colour in this figure legend, the reader is referred to the web version of this article.)

at two different time instances. In Fig. 10a at $t = 1 \times 10^{-4}$ s, the heat loss rate approximately reaches its maximum, then rapidly decreases with time shown in Fig. 10b at $t = 2 \times 10^{-4}$ s. For the regular source, the heat loss rate $\tilde{q}$ is positive, which means the heat is evacuated. In contrast, the heat loss rate $\tilde{q}$ is negative for the image source, signifying a heat gain for the part. When only the regular source I is considered, the total heat loss rate across the curve boundary at $t = 1 \times 10^{-4}$ s is

$$\int_0^{\pi/2} \tilde{q}(x_i) R_c \mathrm{d}\theta = 3.8 \times 10^3\ \mathrm{Js^{-1}m^{-1}}.$$

When the regular and non-modulated image sources are considered, the heat loss rate distribution is less than zero for all values of θ, which means the flux due to the regular source is overcompensated by the non-modulated image source. The total heat loss rate across the curve boundary at $t = 1 \times 10^{-4}$ s is

$$\int_0^{\pi/2} (\tilde{q}(x_i) + \breve{q}(x_i)) R_c \mathrm{d}\theta = -4.8 \times 10^2\ \mathrm{Js^{-1}m^{-1}}.$$

When the regular and modulated image sources are considered, the heat loss rate fluctuates with θ along the boundary. The net heat loss rate along the boundary at $t = 1 \times 10^{-4}$ s becomes

$$\int_0^{\pi/2} (\tilde{q}(x_i) + {}^{\epsilon}\breve{q}(x_i)) R_c \mathrm{d}\theta = 1.1 \times 10^2\ \mathrm{Js^{-1}m^{-1}},$$

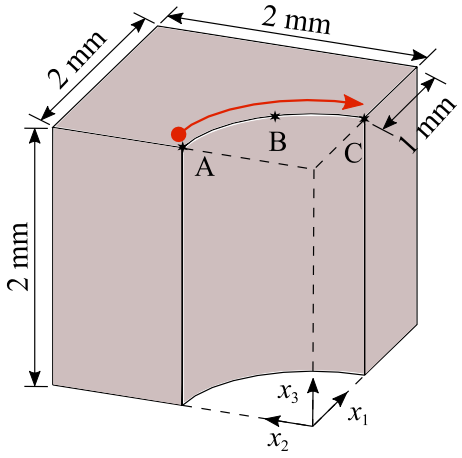

Fig. 11. Single contour line scan along the curved boundary. Temperature histories of points A, B, and C are compared with different temperature decomposition methods.

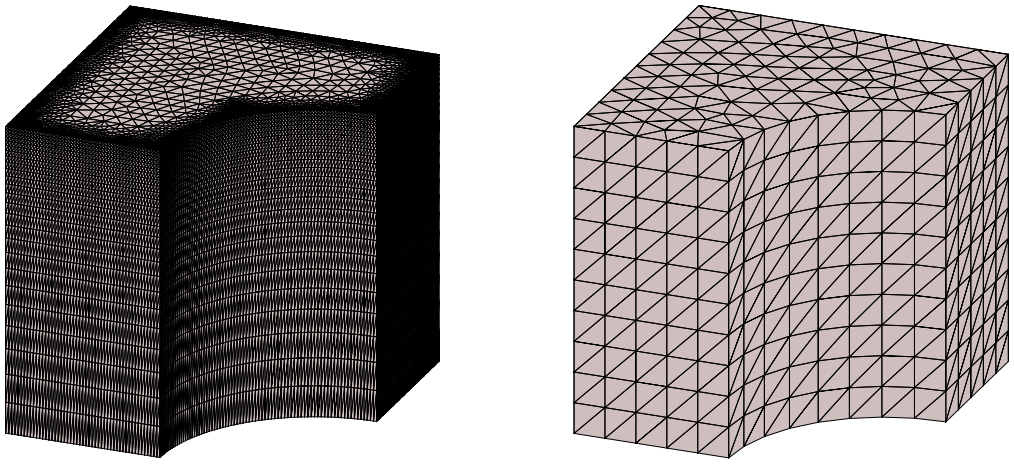

(a) fine mesh (24385 nodes, 102488 elements, average boundary element size 20 μm)

(b) coarse mesh (1264 nodes, 5775 elements, average boundary element size 200 μm).

Fig. 12. Finite element mesh for the contour scan simulation (a) with no image sources where the BCs are enforced numerically through $\hat{T}$, (b) using non-modulated image sources and modulated image sources.

which is around 3% of that of only adopting the regular source. When using the regular and non-modulated image sources, the total heat loss rate across the curved boundary is around 13% of that of only adopting the regular source. Therefore, the adiabatic boundary conditions are better enforced on average using the modulated image source than the non-modulated image source.

It remains to simulate a contour line scanning (discretized into multiple point sources) close to the curved boundary and study the effect of the modulation factor of image sources.

3.2. Single laser scan along a curved boundary

This section aims to compare the effect of multiple image sources with and without modulation in a contour line scan case and study the heat loss rate distribution on the curved boundary. As discussed in Section 2.2, the heat flux component in the outward normal direction given in Eq. (18) is the heat loss rate at a boundary point. The part geometry remains the same, and the laser scan path is shown in Fig. 11. The laser power is taken as 82.5 W, scanning velocity 0.5 m/s, absorptivity fraction 0.77 and laser spot radius 20 μm. The continuous laser scan is discretized into a series of point sources with time intervals of $\Delta t = 1 \times 10^{-5}$ s.[2] The distance between the point sources and the curved boundary is 100 μm. Therefore, the modulation factor remains $\epsilon = 0.86$ for all the modulated image sources.

We compare temperature history and heat loss rate distribution among three distinct temperature decomposition methods. The three points A, B, and C along the boundary depicted in Fig. 11 are used to compare the temperature histories. The first is a reference case using the temperature decomposition method in Eq. (5). The total temperature field is the superposition of the analytical temperature field of regular sources $\tilde{T}$ and the complementary temperature field $\hat{T}$ computed with FEM to impose adiabatic boundary conditions along the curved surface. It should be noted that the $\hat{T}$ field is solved with a time step 1×10^{-4} s larger than the time step to discretize the continuous laser scan. There is no image source in this reference case. Therefore, to achieve adiabatic boundary conditions, the FE mesh should be sufficiently fine, shown in Fig. 12a, to capture

[2] Previous research has proposed that $\Delta t \leq 5 \times 10^{-5}$ s, and we choose a conservative value here.

Table 2
Computation time of the single laser scan along a curved boundary. The calculations are performed on an Intel i7-11850H processor with a clock speed of 2.50 GHz, using a single core, and 16 GB of RAM.

Simulation method	CPU time (s)
Reference	11 450.0
Using non-modulated image sources and linear elements	658.3
Using modulated image sources and linear elements	614.3
Using non-modulated image sources and quadratic elements	1683.6
Using modulated image sources and quadratic elements	1715.7

Table 3
Metrics computed for thermal history differences at Points A, B, and C. The absolute difference of maximum temperatures between the using image sources and reference case is defined as $\Delta T_{\max}$ (°C). The integral of the absolute temperature differences over the full history are defined as $\int |\Delta T| \mathrm{d}t$ (°C · s). The Symmetric Mean Absolute Percentage Error (SMAPE) of temperature histories compared to the reference case. Since the temperature of the build platform is 200 °C, only the data points with temperature higher than 400 °C are used to calculate SMAPE.

Points	Using non-modulated image sources			Using modulated image sources		
	$\Delta T_{\max}$	$\int \lvert\Delta T\rvert \mathrm{d}t$	SMAPE	$\Delta T_{\max}$	$\int \lvert\Delta T\rvert \mathrm{d}t$	SMAPE
A	31.2	4.5×10^{-2}	3.6	16.4	4.1×10^{-2}	2.6
B	43.0	5.9×10^{-2}	1.8	2.7	2.8×10^{-2}	1.4
C	14.6	6.7×10^{-2}	7.8	3.9	4.6×10^{-2}	5.1

the steep temperature gradients and the resulting heat flux due to the regular heat sources. For the reference case, the average element size in the proximity of the boundary is around 20 μm that is equal to the laser spot radius and 10 times smaller than the FE mesh depicted in Fig. 12b utilized for the other two cases with non-modulated and modulated image sources, respectively. In the second and third cases, image sources are introduced to counterbalance the heat flux arising from regular sources. Thus, the resulting temperature gradients due to the regular and image sources are gradual on the part boundary. Both the temperature field $\tilde{T} + \check{T}$ (using image sources without modulation) in the second case, and the temperature field $\tilde{T} + {}^{\epsilon}\check{T}$ (using modulated image sources) in the third case exhibit a smoother profile. As a result, when the boundary condition is enforced with Eq. (14), a much coarser mesh shown in Fig. 12b can be employed, containing around only 5% of the total nodes in the reference case mesh. The total CPU time for the three simulations is given in Table 2. The computational time when adopting image sources is around 5% of the reference case, and there is almost no difference in CPU times between using the modulated and non-modulated image sources.

Usually, the finite element size should be in the same order as the laser spot radius to capture the steep-temperature gradient from the laser spot. Cao et al. [44] adopted a fine element size of 50 μm for the laser spot radius of 70 μm. Roberts et al. [13] adopted the element size as 25 μm when the laser spot radius is 50 μm. Vanini et al. [45] adopted fine element size as 20 μm for laser spot radii of 45 μm and 25 μm. Zhang et al. [46] proposed using fine element size of 5 μm to solve the temperature distribution of laser spot with radius with 50 μm. Consequently, the minimum element size 20 μm used in the reference case (only along the boundaries) is in line with the literature. While using image sources, the element size can be coarsen to 200 μm. As a result, numerical calculations speed up significantly.

The temperature histories of points A, B, and C given in Fig. 11 during the contour laser scanning along the curved surface are shown in Fig. 13 for the three cases. Overall, the temperature histories with modulated image sources (red lines) better approximate the reference temperature history (blue lines). Table 3 gives three measures to evaluate the error of using non-modulated and modulated image sources compared to the reference case. The three measures reported are the absolute difference of peak temperatures with respect to the reference case $\Delta T_{\max}$, the absolute temperature differences over the full history, i.e. $\int |\Delta T| \mathrm{d}t$, and the Symmetric Mean Absolute Percentage Error (SMAPE)[3] of temperature histories. All three measures indicate that modulated image sources lead to a better approximation of the reference case. Moreover, the temperature histories with non-modulated image sources (yellow lines) are consistently overestimated at the three sampling points. Fig. 14 gives snapshots of the temperature field contours of the three temperature decomposition methods at $t = 2 \times 10^{-3}$ s. The temperature isolines are perpendicular to the curved boundary, indicating adiabatic boundary conditions are achieved. Moreover, we compare the area of the layer where the temperature exceeds $T = 1400\,^{\circ}\mathrm{C}$. This area is $2.24 \times 10^{-8}\,\mathrm{m}^2$, $2.77 \times 10^{-8}\,\mathrm{m}^2$ and $2.52 \times 10^{-8}\,\mathrm{m}^2$ respectively in the reference, using non-modulated image sources and using modulated image sources cases. The area in the case of adopting non-modulated image sources is 24% larger than that of the reference case, which indicates that non-modulated image sources lead to an overestimation temperature. While in the reference case and adopting non-modulated image sources, the difference is decreased to 13%. So, we conclude that the modulated image sources can better approximate the temperature history compared to the non-modulated image sources.

Next, we check again the heat loss rate distribution along the curved boundary at $t = 2 \times 10^{-3}$ s in Fig. 15. This is when the temperature at Point B peaks in Fig. 13. Fig. 15a gives the heat loss rate distribution of the reference case, where there is no image source and the finite element size is further decreased to 5 μm near the boundary. The heat loss rate on the curved boundary is

$$\int_0^{\pi/2} (\tilde{q}(x_i) + \hat{q}(x_i)) R_c \mathrm{d}\theta = 4.7 \times 10^3\,\mathrm{J s^{-1} m^{-1}}.$$

Note that the element size around the boundary to acquire accurate q distribution is 5 μm much finer than that of Fig. 12a (20 μm) used for the reference temperature calculation in Figs. 13 and 14a. Further refinement of elements around the boundary from approximately 20 μm to approximately 5 μm makes only 2.6 °C difference for the peak temperature of point B, i.e. convergence of temperature has more lenient spatial discretization requirement than the heat flux. This is reasonable because q represents the heat flux at a specific time step, capturing how much heat is lost at that moment. In contrast, temperature histories show the total change in the system's internal energy, reflecting the cumulative heat losses over time, correlating with the time integration of q. Therefore, a finer mesh must be used to ensure the convergence of the heat loss rate distribution at a specific time step. Fig. 15c illustrates the q distribution when employing the regular sources, modulated image sources, and

[3] SMAPE is a metric that measures the error between two curves or two sets of data points.

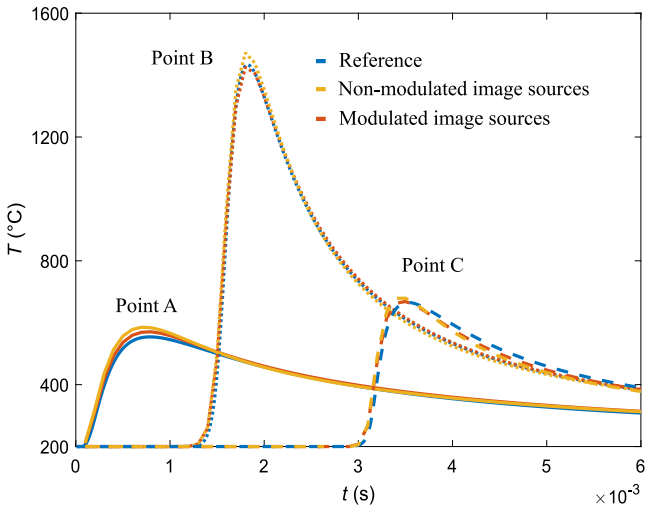

Fig. 13. Comparison of temperature histories by using three temperature decomposition methods. The reference case with no image sources, temperature decomposition $T = \tilde{T} + \hat{T}$; using the non-modulated image source case, temperature decomposition $T = \tilde{T} + \breve{T} + \hat{T}$; using the modulated image source case, temperature decomposition $T = \tilde{T} + {}^{\epsilon}\breve{T} + \hat{T}$. $\hat{T}$ is solved using linear tetrahedron elements (C3D4 element in ABAQUS). (For interpretation of the references to colour in this figure legend, the reader is referred to the web version of this article.)

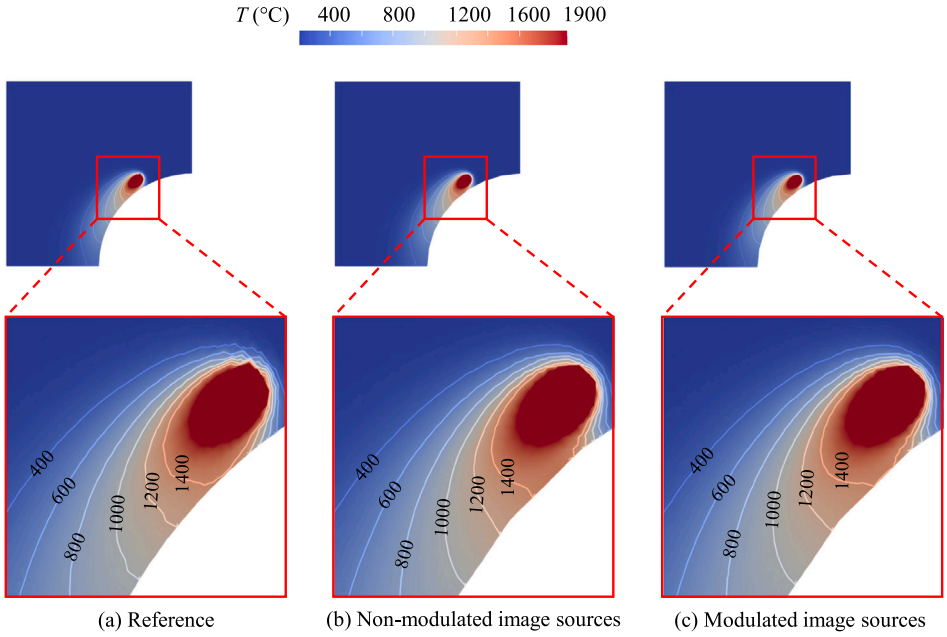

Fig. 14. Temperature distribution at $t = 2 \times 10^{-3}$ s. Three temperature decomposition methods are adopted. Temperature decomposition is $T = \tilde{T} + \hat{T}$ in the reference case. When using non-modulated image sources, temperature decomposition is $T = \tilde{T} + \breve{T} + \hat{T}$. When using modulated image sources, temperature decomposition is $T = \tilde{T} + {}^{\epsilon}\breve{T} + \hat{T}$. The area with $T > 1400\,^{\circ}\mathrm{C}$ is $2.24 \times 10^{-8}\,\mathrm{m}^2$, $2.77 \times 10^{-8}\,\mathrm{m}^2$ and $2.52 \times 10^{-8}\,\mathrm{m}^2$ respectively in the reference, using non-modulated image sources and using modulated image sources cases. (For interpretation of the references to colour in this figure legend, the reader is referred to the web version of this article.)

complementary field ($\tilde{T} + {}^{\epsilon}\breve{T} + \hat{T}$). At the same time, Fig. 15b presents the results obtained with regular sources, image sources, and complementary field ($\tilde{T} + \breve{T} + \hat{T}$). The nine red asterisks represent the angular coordinates of the nine finite element nodes on the curve boundary shown in Fig. 12b. The abrupt change in the heat loss rate at the nodes in Fig. 15b and c is caused by the discontinuity of temperature gradients in the two adjacent linear elements.

Upon using regular and modulated image sources, the modulation factor $\epsilon = 0.86$ scales down the heat loss rate distribution of image sources. The total heat loss rate distribution (purple solid line in Fig. 15c) fluctuates around zero, and the adiabatic boundary conditions are achieved on average. The total heat loss rate across the curve boundary at $t = 2 \times 10^{-3}$ s is

$$\int_0^{\pi/2} (\tilde{q}(x_i) + {}^{\epsilon}\breve{q}(x_i) + \hat{q}(x_i)) R_c \mathrm{d}\theta = -5.7 \times 10^3\,\mathrm{J s^{-1} m^{-1}},$$

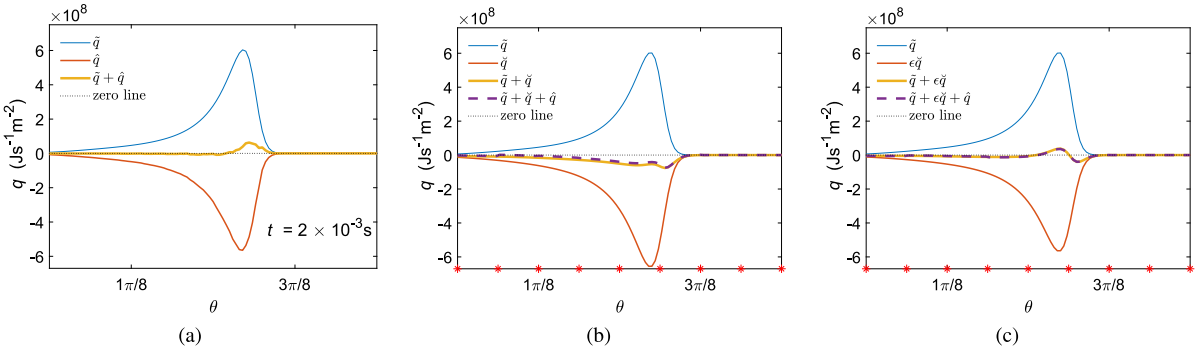

Fig. 15. Heat loss rate distribution q, (a) reference case, the average boundary element size is 5 μm, temperature decomposition $T = \tilde{T} + \hat{T}$, (b) using non-modulated image sources with temperature decomposition $T = \tilde{T} + \breve{T} + \hat{T}$, (c) using modulated image sources with temperature decomposition $T = \tilde{T} + {}^{\epsilon}\breve{T} + \hat{T}$. Heat loss rate distribution due to regular sources $\tilde{q}$, non-modulated image sources $\breve{q}$, modulated image sources ${}^{\epsilon}\breve{q}$, complementary field $\hat{q}$. $\hat{T}$ is solved using linear tetrahedron elements (C3D4 element in ABAQUS). (For interpretation of the references to colour in this figure legend, the reader is referred to the web version of this article.)

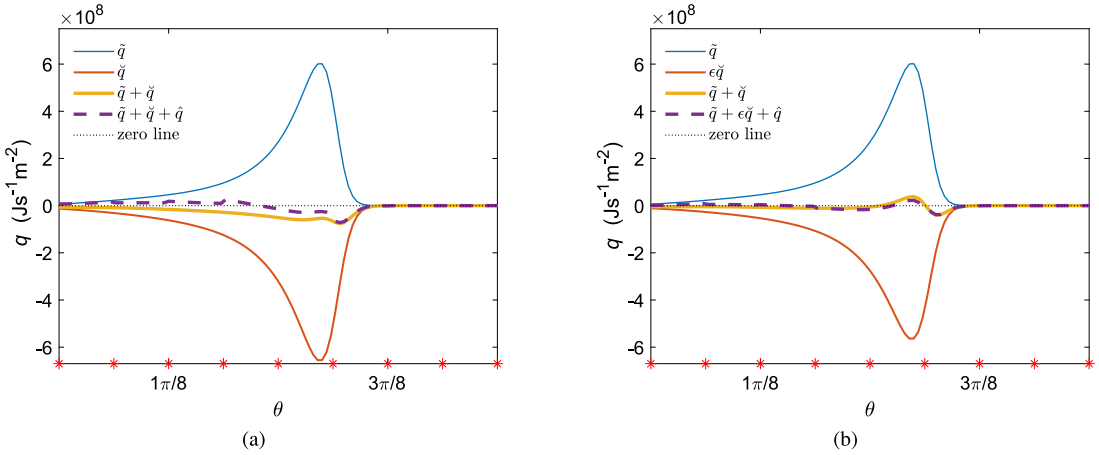

Fig. 16. Heat loss distribution q, (a) using non-modulated image sources with temperature decomposition $T = \tilde{T} + \breve{T} + \hat{T}$ and (b) using modulated image sources with temperature decomposition $T = \tilde{T} + {}^{\epsilon}\breve{T} + \hat{T}$. Heat loss rate distribution due to regular sources $\tilde{q}$, non-modulated image sources $\breve{q}$, and numerical correction ${}^{\epsilon}\breve{q}$; complementary field $\hat{q}$. $\hat{T}$ is solved by using quadratic tetrahedron elements (C3D10 element in ABAQUS). (For interpretation of the references to colour in this figure legend, the reader is referred to the web version of this article.)

where the magnitude is almost the same as the total heat loss rate in the reference case. In contrast, the total heat loss rate distribution (purple solid line in Fig. 15b) is negative for all angular coordinates in the case of having the image sources without modulation since the amount of heat flux across the boundary into the domain is an overestimation, leading to over-heating near the part's boundary. The total heat loss rate across the curve boundary at this time step is

$$\int_0^{\pi/2} (\tilde{q}(x_i) + \breve{q}(x_i) + \hat{q}(x_i)) R_c \mathrm{d}\theta = -2.3 \times 10^4 \,\mathrm{Js^{-1}m^{-1}}.$$

The sign of the heat loss rate indicates a heat gain and the magnitude of the heat gain is one order of magnitude larger than that in the reference case and modulated image source case, which rationalizes higher temperature values in the non-modulated image source case as shown in Fig. 13 and larger high-temperature zones in the non-modulated image source case as shown in Fig. 14. Moreover, we observe that with the given coarse mesh size, the $\hat{q}$ has almost no contribution to the heat loss rate distribution shown in Fig. 15c compared to the effect of $\hat{q}$ in Fig. 15a and b. This also implies that the outgoing heat flux is almost perfectly counter-balanced, and $\hat{q}$ is unnecessary if modulated image sources are used. However, when we adopt p refinement, the same mesh with quadratic shape functions for the tetrahedron elements (C3D10 element in ABAQUS) for computing $\hat{q}$, a more pronounced effect of $\hat{q}$ can be especially seen in Fig. 16a since the non-modulated image sources are inadequate in enforcing the adiabatic boundary condition. The total heat loss rate across the curve boundary at this time step in Fig. 16a is

$$\int_0^{\pi/2} (\tilde{q}(x_i) + \breve{q}(x_i) + \hat{q}(x_i)) R_c \mathrm{d}\theta = -2.2 \times 10^3 \,\mathrm{Js^{-1}m^{-1}},$$

which is one order of magnitude smaller than the total heat flux rate in Fig. 15b, which utilizes linear elements. Thus, now the heat loss rate field $\hat{q}$ more accurately enforces adiabatic conditions in Figs. 16a than 15b with higher order shape functions. For Fig. 16b, the heat loss rate field $\hat{q}$ still does not make a significant contribution, which further indicates that the modulated image sources more accurately enforce the adiabatic boundary conditions better than non-modulated image sources in Fig. 16a. However, it should be noted that the p refinement increases computational time three times as shown in Table 2.

In general, unlike for straight boundaries [42], when we place image sources next to a curved boundary, the adiabatic boundary conditions can only be approximately achieved by modulating the power of image sources in case of a coarse mesh preferred for computational efficiency. The

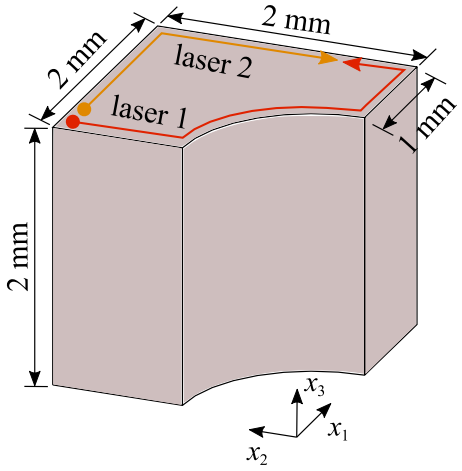

Fig. 17. Schematic illustration of contour scan by two lasers. Scanning of two lasers starts and ends simultaneously, with identical scanning speeds. The two lasers are positioned next to each other at the beginning and end of the scanning process.

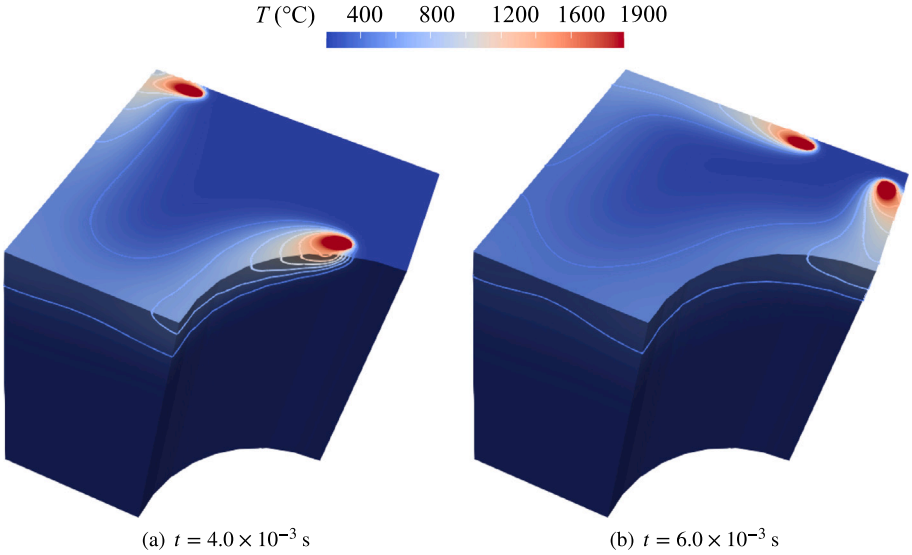

Fig. 18. Snapshots of temperature distribution at (a) $t = 4.0 \times 10^{-3}$ s and (b) $t = 6.0 \times 10^{-3}$ s. Two lasers are scanning simultaneously along the part boundary. (For interpretation of the references to colour in this figure legend, the reader is referred to the web version of this article.)

temperature history shows little difference between the modulated image source and reference cases. Therefore, the adiabatic boundary conditions are easily achieved with a coarse FE mesh comprising linear elements and the modulated image sources. However, when using the image sources without modulation, the image sources overcompensate the heat loss rate from regular sources and lead to an artificial heat gain, thus resulting in larger high-temperature zones. As a result, the modulated image sources more effectively counteract the heat loss, reducing the need for $\hat{q}$ field correction.

3.3. Dual lasers scan along part boundary

In the previous section, we investigated the simulation of a single laser contour scan with the proposed semi-analytical method using modulated image sources that well represent the adiabatic boundary conditions. One key advantage of the semi-analytical method is that no local mesh refinement is needed to follow the laser motion since the steep temperature gradients in the vicinity of the laser beams are captured by analytical fields. Therefore, the semi-analytical method can be readily applied to the simulation of the LPBF process with multiple laser scanning simultaneously with no extra computational cost. In this section, we simulate the contour scanning with two laser beams using the proposed temperature decomposition method $T = \tilde{T} + {}^{e}\breve{T} + \hat{T}$. The laser scanning strategy is shown in Fig. 17. The two lasers start scanning next to each other, scan along the part boundary, and finally meet when the contour scan is complete. The part geometry, laser velocity, laser power, and material thermal properties are the same as those in the previous section. The mesh density is the same as Fig. 12b. For the straight boundaries, we use the image sources without modulation. For the curved boundary, we modulate the image source power according to the radius of curvature. The snapshots of temperature fields at two instances are shown in Fig. 18. It can be observed that the temperature isolines remain perpendicular to straight and curved boundaries, which indicates adiabatic boundary conditions are enforced. Moreover, the number of simultaneously acting lasers can be increased with no additional computational cost.

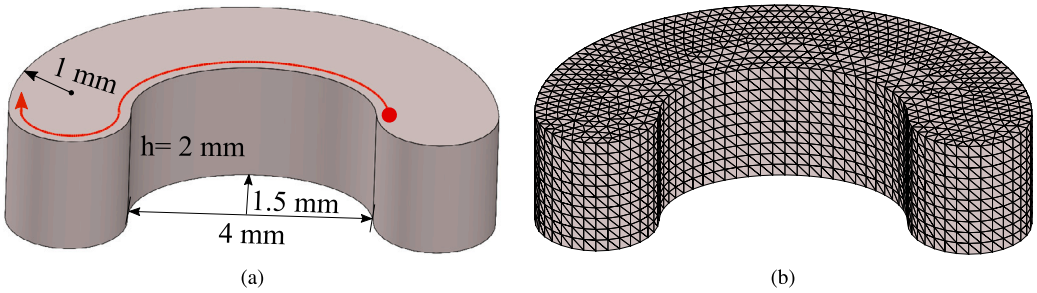

Fig. 19. (a) elliptic part geometry with changing local radii of curvature. The model plane boundary is constructed by two elliptical and circular arcs. (b) discretization of the part with finite elements with an average element size 200 μm.

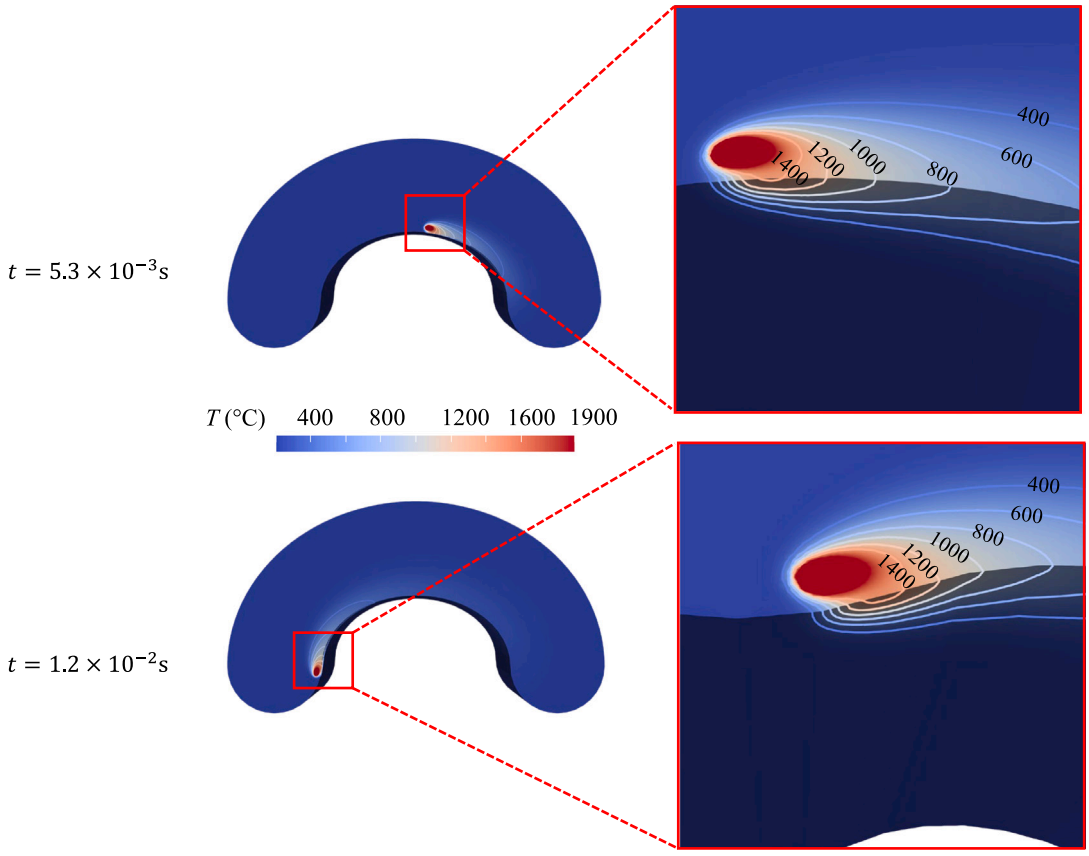

Fig. 20. Snapshots of temperature distribution at $t = 5.3 \times 10^{-3}$ s and $t = 1.2 \times 10^{-2}$ s during a single laser scanning along the edge of an elliptic part. (For interpretation of the references to colour in this figure legend, the reader is referred to the web version of this article.)

3.4. Scanning along an elliptic boundary

In the preceding sections, we discussed using image sources along an arc boundary with a constant radius of curvature, and a constant power modulation factor can be calculated from Eq. (23) for all image sources. In this section, we consider applying the proposed method to elliptic boundaries with gradually varying radius of curvature, shown in Fig. 19a. The laser parameters and material properties are the same as above. A laser scanning along the edge of the part is also depicted in Fig. 19a. The part is meshed with linear tetrahedral elements with an average size 0.2 mm, which is ten times larger than the laser spot radius, as shown in Fig. 19b. We use osculating circles shown in Fig. 6 to approximate the local curvature of the ecliptic boundaries and calculate the image source modulation factors based on the relative position of the regular source, osculating circles and image source positions as discussed in Section 2.3. The temperature fields at $t = 5.3 \times 10^{-3}$ s and $t = 1.2 \times 10^{-2}$ s are shown in Fig. 20. At $t = 5.3 \times 10^{-3}$ s, the laser is scanning along the elliptic boundary, while at $t = 1.2 \times 10^{-2}$ s, the laser transitions between the arc boundary and elliptic boundary. Observe that the isolines of the temperature field are perpendicular to the part edge, which indicates that the adiabatic boundary conditions are satisfied for both time instances. Through the numerical example in the section, it can be demonstrated that our method can applied to non-constant curvature boundaries.

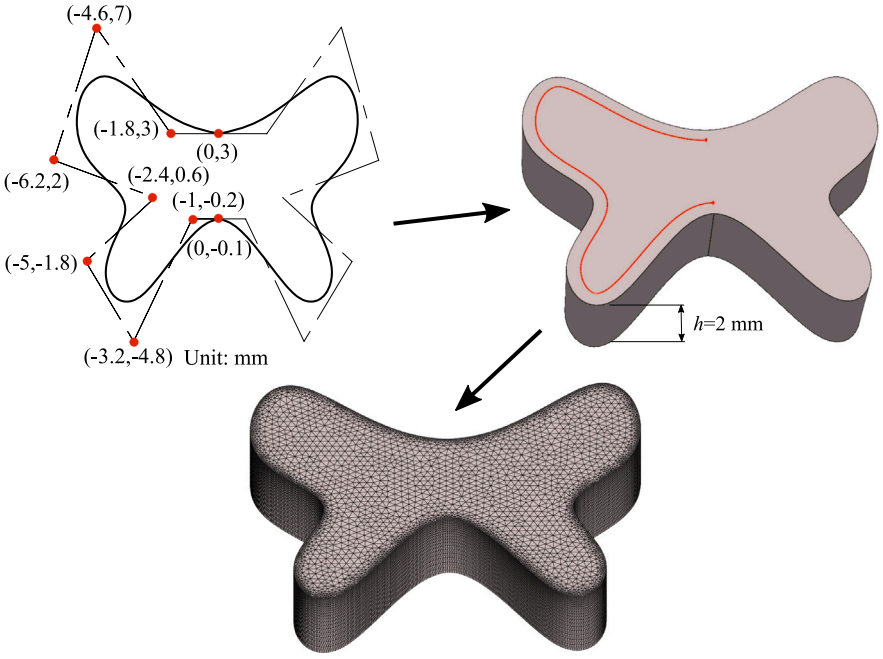

Fig. 21. A butterfly-shaped boundary constructed by B-spline curves and control points. The 3D STL file for the butterfly-shaped part is created through the extrusion of the boundary. The laser scan path is on top of the 3D part. To simulate the temperature history, the 3D part is discretized using linear tetrahedron elements (C3D4 element in ABAQUS), and the boundary element size is approximately 20 μm.

3.5. Scanning along a geometrically complex part constructed by B-splines

In this section, we simulate a scanning process on a more complicated butterfly geometry shown in Fig. 21, constructed by cubic B-splines and control points. The laser scans along the part boundary consisting of concave and convex boundary segments. First, we offset the points on the B-spline boundary using Eq. (28). Through parameterization, we get a continuous laser scan path. Then, the continuous laser line scan is discretized into a series of equidistant point heat sources by using arc-length parameterization and solving the constrained optimization problem given in Eq. (C.11). Following the procedure shown in Fig. 6, the image source positions are determined by osculating circles and corresponding regular source positions, with the modulation factors calculated according to local radii of curvatures with Eqs. (22) and (23).

Similarly, two temperature decomposition methods are adopted in this section. The first serves as a case where the temperature decomposition $T = \tilde{T} + \hat{T}$ is used with the element size of approximately 20 μm near the boundary as shown in Fig. 21. The second method is the proposed method in this paper, i.e., $T = \tilde{T} + {}^{\epsilon}\check{T} + \hat{T}$ where modulated image sources are incorporated. A non-zero value for the complementary field $\hat{T}$ compensates for the heat loss rate from the regular sources in the reference case (without image sources). To examine the extent to which the modulated image source can make $\hat{T}$ field redundant, the same fine mesh is also utilized with the proposed method in this paper. Fig. 22 gives the temperature distribution at $t = 0.020$ s in the case of using the modulated image sources, where the temperature isolines are perpendicular to the boundaries and hence adiabatic boundary conditions are satisfied. Fig. 23 provides the FEM solutions of complementary field $\hat{T}$ for the two cases. In the reference case, Fig. 23a, since no image sources are adopted, $\hat{T}$ field needs to correct for the heat loss rate (or heat flux in the surface outward normal direction) due to regular sources to achieve adiabatic boundary conditions. As a result, the contribution of $\hat{T}$ to the overall temperature prediction is necessary. Fig. 23b shows the $\hat{T}$ temperature distribution where the total temperature field is decomposed using $T = \tilde{T} + {}^{\epsilon}\check{T} + \hat{T}$. The modulated image sources compensate for the heat loss rate across the boundary due to regular sources to enforce adiabatic boundary conditions. Then, the contribution of $\hat{T}$ to the overall temperature prediction is almost negligible. This implies the utilization of modulated image sources can almost perfectly approximate adiabatic boundary conditions for a geometrically complex boundary, thereby allowing for the use of a coarser mesh in FEM to solve the $\hat{T}$ field for higher computational efficiency.

4. Discussion

We have proposed a method to modulate the power of image sources to enforce the adiabatic boundary conditions. This modulation factor accounts for the radii of curvature along the boundary curves, enabling the modulated image sources to effectively offset the heat loss rate due to regular sources near the local boundary. This approach reduces the integrated heat loss across the local boundary to zero. However, the resulting net heat loss rate distribution from the regular and modulated image sources still fluctuates along the part boundary.

According to Saint-Venant's Principle, this redistribution of heat loss rate around the boundary will influence the temperature field less when sampling points are away from the current laser scanning area [47,48]. Furthermore, the amount of redistributed heat loss rate accounts for a small proportion of the heat loss rate from regular sources, meaning that the modulated image sources effectively compensate the heat loss rate from regular sources. As a result, even when sampling points are close to the laser scan path, the temperature history will have negligible differences compared with the reference case. The difference of maximum temperature is as small as 2.7 °C. Besides, the maximum SMAPE is within 5.1%, indicating a good agreement with the reference temperature histories. In contrast, when non-modulated image sources are used, the peak temperature deviates by 43.0 °C from the reference case. This suggests that the non-modulated image sources may also be an alternative option to coarsen the mesh and alleviate computational costs while maintaining certain acceptable accuracy.

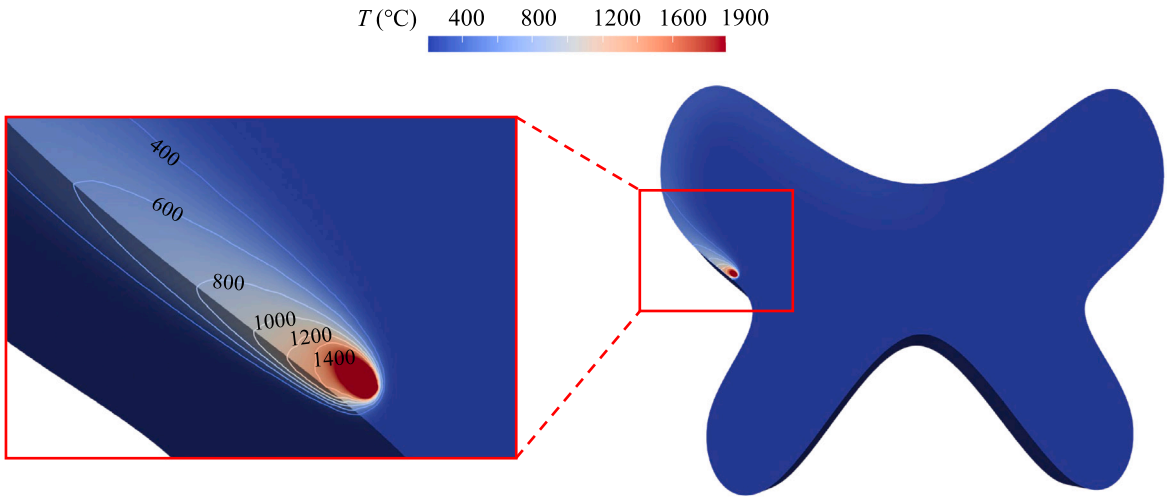

Fig. 22. Temperature distribution at $t = 0.020$ s. The temperature decomposition $T = \tilde{T} + {}^{e}\check{T} + \hat{T}$ is adopted with modulated image sources. (For interpretation of the references to colour in this figure legend, the reader is referred to the web version of this article.)

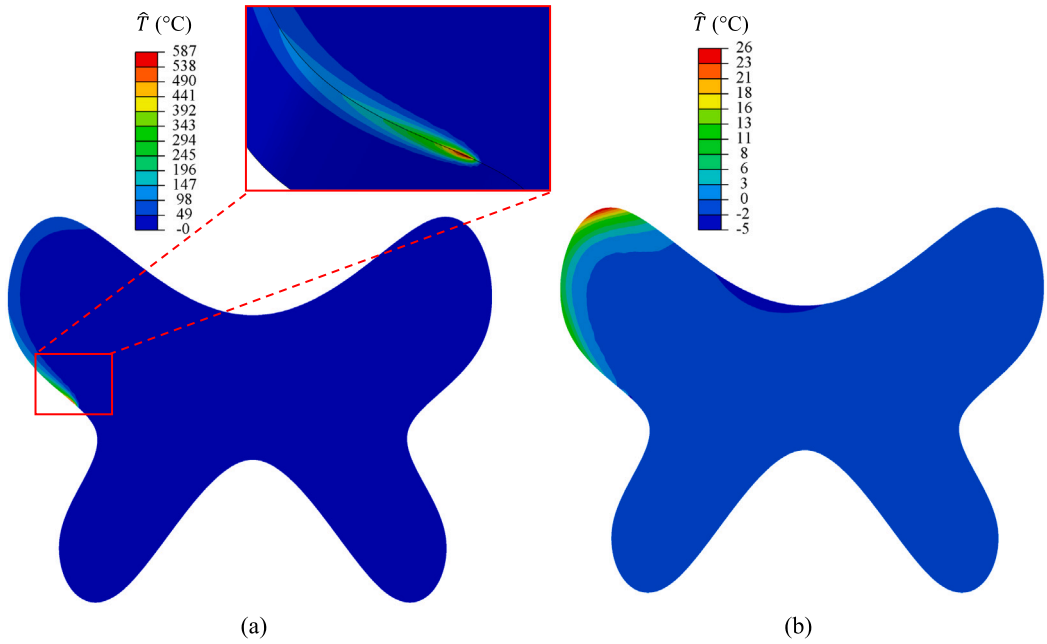

Fig. 23. $\hat{T}$ complementary field at $t = 0.020$ s. (a) without image sources and the temperature field is decomposed using $T = \tilde{T} + \hat{T}$. (b) using the modulated image sources, and the temperature field is decomposed using $T = \tilde{T} + {}^{e}\check{T} + \hat{T}$. (For interpretation of the references to colour in this figure legend, the reader is referred to the web version of this article.)

Adiabatic boundary conditions are assumed on the powder-part boundary in this paper. However, in the LPBF process, a small amount of heat is conducted to the surrounding powder. The proposed method can also be applied under the low boundary conductivity consideration. In this case, the modulated image sources should partly compensate for the regular source's heat loss rate to approximate the powder-part boundary's real heat loss rate. Besides, this paper proposes that an image source should be induced when the distance of a regular source to the boundary is proposed to be less than $15r$. This method, in principle, can be applied in the thermal simulation of 3D print structures with small cross sections, such as thin walls or lattice structures (one dimension less than $30r$). However, boundaries on the opposite side of a structure can be close to each other. As discussed in [26], more image sources corresponding to the same regular source through multi-reflection along the boundaries should be included.

5. Conclusions

The semi-analytical method is a fast part-scale thermal simulation approach for the LPBF process. This method requires a complementary field to enforce the boundary conditions. To solve the complementary field numerically, the traditional semi-analytical method requires spatial discretization on part boundaries to be as fine as the laser spot radius. Consequently, the computational efficiency of the method is limited due to the excessive degrees of freedom.

In this paper, we propose incorporating image sources to compensate for the heat loss from regular heat sources representing laser scanning at the powder-part boundary. The powder-part boundary is assumed to be adiabatic. The positions and intensity of image sources can be easily determined for straight boundaries. However, utilizing image sources for curved boundaries, commonly the case for intricate parts additively manufactured, was an open question.

In our novel method, image source power is modulated according to image position and local radius of curvature near a curved boundary to almost perfectly compensate for the heat flux emanating from laser-associated point heat sources. In this way, the numerical temperature field to be solved becomes smoother, and hence, we can coarsen the mesh for the numerical correction field around 10 times on the part boundary. Therefore, the computational efficiency can be increased by 20 times.

The peak temperature difference between the reference case and the simulation with modulated image sources is as small as several degrees. In contrast, the difference with the non-modulated case becomes 43.0 °C. Furthermore, the semi-analytical method employed in this paper is suitable for multiple laser scans acting simultaneously, obviating the need for local mesh refinement based on the laser scanning path. This capability further contributes to the computational efficiency of the proposed method with no additional cost.

Despite the promising results, this study has limitations. The temperature-independent thermal properties of Ti6Al4V are assumed to make use of the superposition principle, which may introduce certain deviations depending on the temperature dependence of the material used.

CRediT authorship contribution statement

Y. Yang: Writing – review & editing, Writing – original draft, Software, Methodology, Data curation, Conceptualization. **Y. Ji:** Writing – review & editing, Writing – original draft, Software, Methodology, Data curation, Conceptualization. **M. Möller:** Writing – review & editing, Methodology, Conceptualization. **C. Ayas:** Writing – review & editing, Writing – original draft, Software, Methodology, Conceptualization.

Declaration of competing interest

The authors declare that they have no known competing financial interests or personal relationships that could have appeared to influence the work reported in this paper.

Acknowledgment

The authors would like to thank Prof. Fred van Keulen for his valuable suggestions. Yang Yang is supported by China Scholarship Council (No. 202106150031).

Appendix A

We introduce the time delay $r^2/8\alpha$ for a point source to represent a 3D Gaussian laser source. Mathematically, the temperature fields are the same due to the two kinds of sources. Firstly, consider a point source with the time delay, Eq. (7) is written as

$$\tilde{T}^{(I)}(x_i,t)=\frac{QA}{4\rho c_p(\pi\alpha(t-\tilde{t}^{(I)}+r^2/8\alpha))^{\frac{3}{2}}}\exp\left(\frac{-(R^{(I)})^2}{4\alpha(t-\tilde{t}^{(I)}+r^2/8\alpha)}\right). \tag{A.1}$$

Now, we consider a 3D Gaussian source activated at $t=\tilde{t}^{(I)}$ with energy distribution as

$$q(x_i)=\frac{2Q}{\sigma^3\pi\sqrt{\pi}}\exp\left(-\frac{(R^{(I)})^2}{\sigma^2}\right). \tag{A.2}$$

$x_i^{(I)}$ is the center of the Gaussian source. The distance between the point of interest and the Gaussian source center is $R^{(I)}$. $\sigma=r/\sqrt{S_f}$, and r is the laser spot radius. The Gaussian source's shape factor, determining the energy concentration, is denoted with S_f. The temperature distribution due to the Gaussian source is by integration of the temperature field of the distributed input energy

$$\begin{aligned}T(x_i,t)=&\frac{2QA}{\sigma^3\pi\sqrt{\pi}}\\&\int_{-\infty}^{\infty}\int_{-\infty}^{\infty}\int_{-\infty}^{x_3^{(I)}}\exp\left(-\frac{(x_1'-x_1^{(I)})^2+(x_2'-x_2^{(I)})^2+(x_3'-x_3^{(I)})^2}{\sigma^2}\right)\\&\frac{\exp(\frac{-(R')^2}{4\alpha(t-\tilde{t}^{(I)})})}{4\rho c_p(\pi\alpha(t-\tilde{t}^{(I)}))^{\frac{3}{2}}}\mathrm{d}x_1'\mathrm{d}x_2'\mathrm{d}x_3',\end{aligned} \tag{A.3}$$

where

$$R'=\sqrt{(x_1-x_1')^2+(x_2-x_2')^2+(x_3-x_3')^2}. \tag{A.4}$$

The integration has the close-form

$$T(x_i,t)=\frac{2QA}{\rho c_p\pi\sqrt{\pi}}\frac{1}{(4\alpha(t-\tilde{t}^{(I)})+\sigma^2)^{(3/2)}}\exp\left(\frac{-(R^{(I)})^2}{4\alpha(t-\tilde{t}^{(I)})+\sigma^2}\right). \tag{A.5}$$

When $S_f=2$, Eq. (A.5) is the same as Eq. (A.1).

Appendix B

A net zero heat loss through the arc segment of θ_0 near the regular source can be achieved. At the point on the arc boundary with θ_0, the temperature decreased to e^{-3} of the temperature at point p Fig. 5. This value is chosen to capture high-temperature zones and make subsequent derivation easy. Certainly, the ratio of the temperatures between the two points can be smaller with larger θ_0. The points on the boundary segment with $x_1 = R_c\cos\theta$ and $x_2 = R_c\sin\theta$, the heat loss rate across the boundary segment due to the regular source I at time t is written as an integral

$$\tilde{g}^{(I)}(\theta_0,t) = \int_0^{\theta_0} \frac{\nu}{(t-\tilde{\tau}^{(I)})^{(3/2)}} \exp\left(\frac{-(R_c\cos\theta-\tilde{x}_1^{(I)})^2-(R_c\sin\theta-\tilde{x}_2^{(I)})^2}{4\alpha(t-\tilde{\tau}^{(I)})}\right)\left(\frac{-2\tilde{x}_1^{(I)}R_c\cos\theta-2\tilde{x}_2^{(I)}R_c\sin\theta+2R_c^2}{4\alpha(t-\tilde{\tau}^{(I)})R_c}\right)R_c\mathrm{d}\theta. \tag{B.1}$$

Since the regular source I is located at $(R_c-d,0,0)$. Then, Eq. (B.1) becomes

$$\tilde{g}^{(I)}(\theta_0,t) = \int_0^{\theta_0} \frac{\nu}{(t-\tilde{\tau}^{(I)})^{(3/2)}} \exp\left(\frac{-(R_c-d)^2-R_c^2+2R_c(R_c-d)\cos\theta}{4\alpha(t-\tilde{\tau}^{(I)})}\right)\left(\frac{-(R_c-d)R_c\cos\theta+R_c^2}{2\alpha(t-\tilde{\tau}^{(I)})}\right)\mathrm{d}\theta. \tag{B.2}$$

Integrating the heat loss rate of the line along the x_3 direction yields

$$\begin{aligned}\tilde{\phi}^{(I)}(\theta_0,t) &= \tilde{g}^{(I)}(\theta_0,t)\int_{-\infty}^{\tilde{x}_3^{(I)}} \exp\left(\frac{-(x_3-\tilde{x}_3^{(I)})^2}{4\alpha(t-\tilde{\tau}^{(I)})}\right)\mathrm{d}x_3\\ &= \sqrt{\pi\alpha(t-\tilde{\tau}^{(I)})}\tilde{g}^{(I)}(\theta_0,t),\end{aligned} \tag{B.3}$$

where $-\infty$ and $\tilde{x}_3^{(I)}$ are the lower and upper limits of the integral. Similarly, for the image source J located at $(R_c+d,0,0)$, the heat loss rate across the boundary segment due to the image source J at time t is

$$\breve{g}^{(J)}(\theta_0,t) = \int_0^{\theta_0} \frac{\epsilon^{(J)}\nu}{(t-\breve{\tau}^{(J)})^{(3/2)}} \exp\left(\frac{-(R_c+d)^2-R_c^2+2R_c(R_c+d)\cos\theta}{4\alpha(t-\breve{\tau}^{(J)})}\right)\left(\frac{-(R_c+d)R_c\cos\theta+R_c^2}{2\alpha(t-\breve{\tau}^{(J)})}\right)\mathrm{d}\theta. \tag{B.4}$$

the integration of the heat loss rate through the same boundary area is written as

$$\begin{aligned}\breve{\phi}^{(J)}(\theta_0,t) &= \breve{g}^{(J)}(\theta_0,t)\int_{-\infty}^{\breve{x}_3^{(J)}} \exp\left(\frac{-(x_3-\breve{x}_3^{(J)})^2}{4\alpha(t-\breve{\tau}^{(J)})}\right)\mathrm{d}x_3,\\ &= \sqrt{\pi\alpha(t-\breve{\tau}^{(J)})}\breve{g}^{(J)}(\theta_0,t).\end{aligned} \tag{B.5}$$

The activation time of regular source I and image source J are identical, (i.e. $\breve{\tau}^{(J)} = \tilde{\tau}^{(I)}$ in Eqs. (B.3) and (B.5)). For both regular and image sources, the heat loss rate proportionally changes in the x_3 direction. When $|\breve{\phi}^{(J)}| = |\tilde{\phi}^{(I)}|$, the net heat loss rate over the boundary segment is zero, and the adiabatic boundary conditions are achieved on average. However, we need to integrate the heat loss rate in time to enforce a net zero heat loss over time. For the regular source I, integrate the heat loss rate of the lateral surface in Eq. (B.3) on a time duration

$$\tilde{\boldsymbol{\Phi}}^{(I)} = \int_{t_s}^{t_e}\int_0^{\theta_0} \frac{\nu\sqrt{\pi\alpha}}{t-\tilde{\tau}^{(I)}} \exp\left(\frac{-(R_c-d)^2-R_c^2+2R_c(R_c-d)\cos\theta}{4\alpha(t-\tilde{\tau}^{(I)})}\right)\left(\frac{-(R_c-d)R_c\cos\theta+R_c^2}{2\alpha(t-\tilde{\tau}^{(I)})}\right)\mathrm{d}\theta\mathrm{d}t, \tag{B.6}$$

where t_s is the starting time for heat loss calculation, and t_e is the end time. t_s and t_e should capture the period when steep temperature gradients happen on the part boundary due to the laser sources. We propose the integral bounds as $t_s = \tilde{\tau}^{(I)} + d^2/10\alpha$ and $t_e = \tilde{\tau}^{(I)} + d^2/\alpha$. At $t = t_e$, the flux at $(R_c,0)$ decreases to less than 5% of its peak value at $t = t_s$ from Eq. (18). After t_f, the temperature field due to the regular source is sufficiently smooth to be captured numerically. For the image source, the heat loss within a time duration is written as

$$\breve{\boldsymbol{\Phi}}^{(J)} = \int_{t_s}^{t_e}\int_0^{\theta_0} \frac{\epsilon^{(J)}\nu\sqrt{\pi\alpha}}{t-\breve{\tau}^{(J)}} \exp\left(\frac{-(R_c+d)^2-R_c^2+2R_c(R_c+d)\cos\theta}{4\alpha(t-\breve{\tau}^{(J)})}\right)\left(\frac{-(R_c+d)R_c\cos\theta+R_c^2}{2\alpha(t-\breve{\tau}^{(J)})}\right)\mathrm{d}\theta\mathrm{d}t. \tag{B.7}$$

To enforce $|\tilde{\boldsymbol{\Phi}}^{(I)}| = |\breve{\boldsymbol{\Phi}}^{(J)}|$ for the approximate adiabatic boundary conditions, $\epsilon^{(J)}$ is given as

$$\epsilon^{(J)} = \left|\frac{\int_{t_s}^{t_e}\int_0^{\theta_0} \frac{\nu\sqrt{\pi\alpha}}{t-\tilde{\tau}^{(I)}} \exp\left(\frac{-(R_c-d)^2-R_c^2+2R_c(R_c-d)\cos\theta}{4\alpha(t-\tilde{\tau}^{(I)})}\right)\left(\frac{-(R_c-d)R_c\cos\theta+R_c^2}{2\alpha(t-\tilde{\tau}^{(I)})}\right)\mathrm{d}\theta\mathrm{d}t}{\int_{t_s}^{t_e}\int_0^{\theta_0} \frac{\nu\sqrt{\pi\alpha}}{t-\breve{\tau}^{(J)}} \exp\left(\frac{-(R_c+d)^2-R_c^2+2R_c(R_c+d)\cos\theta}{4\alpha(t-\breve{\tau}^{(J)})}\right)\left(\frac{-(R_c+d)R_c\cos\theta+R_c^2}{2\alpha(t-\breve{\tau}^{(J)})}\right)\mathrm{d}\theta\mathrm{d}t}\right|. \tag{B.8}$$

The $\epsilon^{(J)}$ in Eq. (B.8) is simplified as:

$$\epsilon^{(J)} = \left|\frac{\int_{t_s}^{t_e}\int_0^{\theta_0} \frac{1}{t-\tilde{\tau}^{(I)}} \exp\left(\frac{-(R_c-d)^2-R_c^2+2R_c(R_c-d)\cos\theta}{4\alpha(t-\tilde{\tau}^{(I)})}\right)\left(\frac{-(R_c-d)R_c\cos\theta+R_c^2}{2\alpha(t-\tilde{\tau}^{(I)})}\right)\mathrm{d}\theta\mathrm{d}t}{\int_{t_s}^{t_e}\int_0^{\theta_0} \frac{1}{t-\breve{\tau}^{(J)}} \exp\left(\frac{-(R_c+d)^2-R_c^2+2R_c(R_c+d)\cos\theta}{4\alpha(t-\breve{\tau}^{(J)})}\right)\left(\frac{-(R_c+d)R_c\cos\theta+R_c^2}{2\alpha(t-\breve{\tau}^{(J)})}\right)\mathrm{d}\theta\mathrm{d}t}\right|. \tag{B.9}$$

Assuming $t_0 = \tilde{\tau}^{(I)} = \breve{\tau}^{(J)}$. Then, $t_s - t_0 = \frac{d^2}{10\alpha}$, $t_e - t_0 = \frac{d^2}{\alpha}$.

$$\epsilon^{(J)} = \left|\frac{\int_{t_s}^{t_e}\int_0^{\theta_0} \frac{1}{t-t_0} \exp\left(\frac{-d^2}{4\alpha(t-t_0)}\right)\exp\left(\frac{R_c(R_c-d)(\cos\theta-1)}{2\alpha(t-t_0)}\right)\left(\frac{-(R_c-d)R_c\cos\theta+R_c^2}{2\alpha(t-t_0)}\right)\mathrm{d}\theta\mathrm{d}t}{\int_{t_s}^{t_e}\int_0^{\theta_0} \frac{1}{t-t_0} \exp\left(\frac{-d^2}{4\alpha(t-t_0)}\right)\exp\left(\frac{R_c(R_c+d)(\cos\theta-1)}{2\alpha(t-t_0)}\right)\left(\frac{-(R_c+d)R_c\cos\theta+R_c^2}{2\alpha(t-t_0)}\right)\mathrm{d}\theta\mathrm{d}t}\right|. \tag{B.10}$$

The ratio of integrated heat flux due to a regular source and an image source $\epsilon^{(J)}(t)$ at time t is written as

$$\epsilon^{(J)}(t) = \left| \frac{\int_0^{\theta_0} \frac{1}{t-t_0} \exp\left(\frac{R_c(R_c-d)(\cos\theta-1)}{2\alpha(t-t_0)}\right)\left(\frac{-(R_c-d)R_c\cos\theta+R_c^2}{2\alpha(t-t_0)}\right)\mathrm{d}\theta}{\int_0^{\theta_0} \frac{1}{t-t_0} \exp\left(\frac{R_c(R_c+d)(\cos\theta-1)}{2\alpha(t-t_0)}\right)\left(\frac{-(R_c+d)R_c\cos\theta+R_c^2}{2\alpha(t-t_0)}\right)\mathrm{d}\theta} \right|, \tag{B.11}$$

and defining the term $\tilde{L}^{(I)}(t,\theta_0)$ and $\check{L}^{(J)}(t,\theta_0)$ as

$$\tilde{L}^{(I)}(t,\theta_0) = \int_0^{\theta_0} \exp\left(\frac{R_c(R_c-d)(\cos\theta-1)}{2\alpha(t-t_0)}\right)\left(\frac{-(R_c-d)R_c\cos\theta+R_c^2}{2\alpha(t-t_0)}\right)\mathrm{d}\theta, \tag{B.12}$$

$$\check{L}^{(J)}(t,\theta_0) = \int_0^{\theta_0} \exp\left(\frac{R_c(R_c+d)(\cos\theta-1)}{2\alpha(t-t_0)}\right)\left(\frac{-(R_c+d)R_c\cos\theta+R_c^2}{2\alpha(t-t_0)}\right)\mathrm{d}\theta. \tag{B.13}$$

Eq. (B.12) is rewritten as

$$\tilde{L}^{(I)}(\mu,\theta_0) = \int_0^{\theta_0} \exp\left(\mu(\cos\theta-1)\right)\left(-\mu\cos\theta+\frac{R_c^2}{2\alpha(t-t_0)}\right)\mathrm{d}\theta, \tag{B.14}$$

where $\mu = \frac{R_c(R_c-d)}{2\alpha(t-t_0)}$. To determine the upper bound of the integration, define

$$\tilde{M}^{(I)}(\theta) = \exp\left(\frac{R_c(R_c-d)(\cos\theta-1)}{2\alpha(t-t_0)}\right), \tag{B.15}$$

θ_0 satisfy the criteria

$$\frac{\tilde{M}^{(I)}(\theta_0)}{\tilde{M}^{(I)}(0)} = \exp\left(\frac{R_c(R_c-d)(\cos\theta_0-1)}{2\alpha(t-t_0)}\right) = e^{-3}. \tag{B.16}$$

Then,

$$\frac{R_c(R_c-d)(\cos\theta_0-1)}{2\alpha(t-t_0)} = -3, \tag{B.17}$$

which is

$$\mu(\cos\theta_0-1) = -3. \tag{B.18}$$

Let $p = \mu(-\cos\theta+1)$, then Eq. (B.14) is rewritten as

$$\tilde{L}^{(I)} = \int_0^{\mu(-\cos\theta_0+1)} e^{-p}\left(p+\frac{R_c d}{2\alpha(t-t_0)}\right)\frac{\mathrm{d}p}{\mu\sin\theta}, \tag{B.19}$$

where $\cos\theta = 1-\frac{p}{\mu}$ and $\sin\theta = \frac{\sqrt{2p\mu-p^2}}{\mu}$, and $\tilde{L}^{(I)}$ is rewritten as

$$\tilde{L}^{(I)} = \int_0^{\mu(-\cos\theta_0+1)} e^{-p}\left(p+\frac{R_c d}{2\alpha(t-t_0)}\right)\frac{\mathrm{d}p}{\sqrt{2p\mu-p^2}}. \tag{B.20}$$

Since $p \ll \mu$,

$$\tilde{L}^{(I)} = -\frac{1}{\sqrt{\mu}}\int_0^{\mu(-\cos\theta_0+1)} e^{-p}\left(p+\frac{R_c d}{2\alpha(t-t_0)}\right)\frac{1}{\sqrt{2p}}\mathrm{d}p, \tag{B.21}$$

$$\tilde{L}^{(I)} = -\frac{1}{\sqrt{2\mu}}\int_0^{3} (e^{-p})\sqrt{p}+\frac{R_c d}{2\alpha(t-t_0)}\frac{e^{-p}}{\sqrt{p}}\mathrm{d}p. \tag{B.22}$$

Similarly for the image source, Eq. (B.13) is written as

$$\check{L}^{(J)} = -\frac{1}{\sqrt{2\lambda}}\int_0^{3\frac{R_c+d}{R_c-d}} (e^{-p})\sqrt{q}-\frac{R_c d}{2\alpha(t-t_0)}\frac{e^{-q}}{\sqrt{q}}\mathrm{d}q, \tag{B.23}$$

where $\lambda = \frac{R_c(R_c+d)}{2\alpha(t-t_0)}$ and $q = \lambda(-\cos\theta+1)$. Then, we have

$$\frac{\tilde{L}^{(I)}}{\check{L}^{(J)}} = \frac{\frac{1}{\sqrt{2\mu}}\int_0^{3} (e^{-p})\sqrt{p}+\frac{R_c d}{2\alpha(t-t_0)}\frac{e^{-p}}{\sqrt{p}}\mathrm{d}p}{\frac{1}{\sqrt{2\lambda}}\int_0^{3\frac{R_c+d}{R_c-d}} (e^{-q})\sqrt{q}-\frac{R_c d}{2\alpha(t-t_0)}\frac{e^{-q}}{\sqrt{p}}\mathrm{d}q}. \tag{B.24}$$

Since $R_c \gg d$, $\frac{R_c+d}{R_c-d} \approx 1$, integration of Eq. (B.24) leads to

$$\frac{\tilde{L}^{(I)}}{\check{L}^{(J)}} = \frac{\frac{1}{\sqrt{2\mu}}\left(k_1+2k_1\frac{R_c d}{2\alpha(t-t_0)}\right)}{\frac{1}{\sqrt{2\lambda}}\left(k_1-2k_1\frac{R_c d}{2\alpha(t-t_0)}\right)}. \tag{B.25}$$

Substitute Eq. (B.25) into Eq. (B.10), and the simplification of Eq. (B.10) leads to

$$\epsilon^{(J)} = \sqrt{\frac{R_c+d}{R_c-d}}\left|\frac{\int_{t_s}^{t_e}\exp\left(\frac{-d^2}{4\alpha(t-t_0)}\right)\left(\frac{1}{t-t_0}+2\frac{R_c d}{2\alpha(t-t_0)^2}\right)dt}{\int_{t_s}^{t_e}\exp\left(\frac{-d^2}{4\alpha(t-t_0)}\right)\left(\frac{1}{t-t_0}-2\frac{R_c d}{2\alpha(t-t_0)^2}\right)dt}\right|, \tag{B.26}$$

$$\epsilon^{(J)} \approx \frac{4R_c+d}{4R_c-d}\sqrt{\frac{R_c+d}{R_c-d}}. \tag{B.27}$$

Appendix C

For a curve degree higher than one, an exact representation of arc-length parameterization is generally unattainable and must be approximated [49]. This part is dedicated to the transformation of the input B-spline curve $\boldsymbol{C}(\xi)$ into its approximate arc-length parameterized form. Such parameterization ensures that any variation within the curve parameter ξ, ranging from 0 to 1 in its parameter space, corresponds to a uniform progression from $\boldsymbol{C}(0)$ to $\boldsymbol{C}(1)$ along the curve path. In other words, incremental advancements in the parameter $\Delta\xi$ yield a sequence of points evenly spaced along the trajectory of the curve.

The "speed" of the parameter, commonly referred to as the Jacobian or the parametric speed of a curve $\boldsymbol{C}$, indicates the rate at which the arc length changes with respect to the curve parameter, denoted $ds/d\xi$. It is mathematically defined as

$$\mathcal{J} = \left\|\frac{d\boldsymbol{x}}{d\xi}\right\|_2 = \sqrt{\left(\frac{dx_1}{d\xi}\right)^2+\left(\frac{dx_2}{d\xi}\right)^2+\left(\frac{dx_3}{d\xi}\right)^2}. \tag{C.1}$$

A constant Jacobian, or uniform parametric speed along the curve, implies that the curve is parameterized linearly with respect to its arc length. Such a parameterization is particularly desirable as it reflects the consistent traversal speed of the laser source. The total arc length L can be evaluated as follows

$$L = \int_0^1 ds = \int_0^1 \left|\boldsymbol{x}'(\xi)\right| d\xi, \tag{C.2}$$

where $\left|\boldsymbol{x}'(\xi)\right| = \sqrt{\left(\frac{dx_1}{d\xi}\right)^2+\left(\frac{dx_2}{d\xi}\right)^2+\left(\frac{dx_3}{d\xi}\right)^2}$ represents the rate of change in arc length, capturing the geometric rate of traversal along the curve.

In the context of an arc-length parameterized curve, the relationship is articulated as

$$\left\|\boldsymbol{x}'(\xi)\right\| = L, \tag{C.3}$$

consistent across all values of the parameter ξ, where

$$L = \int_0^1 \left\|\boldsymbol{x}'(\xi)\right\| \,\mathrm{d}\xi \tag{C.4}$$

defines the total length of the input curve. The ideal extension ratio corresponds to L, given that our parametric domain $\hat{\Omega}$ spans $[0,1]$. For a parametric domain of length L_{param}, this ratio would be appropriately scaled to L/L_{param}.

By integrating the square of the difference between the derivative of the curve, $\left\|\boldsymbol{x}'(\xi)\right\|$, and the total curve length L over its parametric domain and substituting from Eq. (C.4), we obtain

$$\begin{aligned}\int_0^1 \left(\left|x'(\xi)\right| - L\right)^2 d\xi &= \int_0^1 \left|x'(\xi)\right|^2 d\xi - 2L\int_0^1 \left|x'(\xi)\right| d\xi + L^2\int_0^1 1 d\xi \\ &= \int_0^1 \left|x'(\xi)\right|^2 d\xi - L^2.\end{aligned}$$

We define the energy function as follows

$$\mathcal{E}_{\text{ArcLength}} = \frac{1}{L^2}\int_0^1 \left|x'(\xi)\right|^2 d\xi. \tag{C.5}$$

The inclusion of the scaling factor $1/L^2$ in Eq. (C.5) normalizes the convergence criterion across curves with different arc lengths L.

The reparameterization process, illustrated in Fig. 24, establishes a relationship between the original curve parameter ξ and a reparameterized parameter $\hat{\xi}$ via a parameter transfer function

$$\xi = \xi(\hat{\xi}) = \sum_{i=0}^{m}\beta_i N_{i,\hat{p}}(\hat{\xi}), \quad \hat{\xi}\in\hat{\Omega}=[0,1], \tag{C.6}$$

where β_i are control coefficients, and $N_{i,\hat{p}}(\hat{\xi})$ are degree $\hat{p}$ B-spline basis functions.

Consider a parametric curve $\boldsymbol{C}(\xi) = \left[x_1(\xi), x_2(\xi), x_3(\xi)\right]^{\mathrm{T}}$, defined over the interval $\xi\in[0,1]$. This curve can be reparameterized by a parameter transfer function $\xi(\hat{\xi})$, ensuring that $\xi(0)=0$ and $\xi(1)=1$. The reparameterized curve is expressed as

$$\boldsymbol{C}(\xi) = \boldsymbol{C}\left(\xi(\hat{\xi})\right) = \left[x_1\left(\xi(\hat{\xi})\right), x_2\left(\xi(\hat{\xi})\right), x_3\left(\xi(\hat{\xi})\right)\right]^{\mathrm{T}}, \tag{C.7}$$

is referred to as the reparameterization of $\boldsymbol{C}(\xi)$.

Consider the Jacobian matrix of the curve $\boldsymbol{C}$, denoted by $\boldsymbol{\mathcal{J}}_\xi = [x_{1,\xi}, x_{2,\xi}, x_{3,\xi}]^{\mathrm{T}}$. Assuming $\boldsymbol{\mathcal{J}}_\xi^{\mathrm{T}}\boldsymbol{\mathcal{J}}_\xi = x_{1,\xi}^2 + x_{2,\xi}^2 + x_{3,\xi}^2 > 0$, we obtain $\boldsymbol{\mathcal{J}}_{\hat{\xi}}^{\mathrm{T}}\boldsymbol{\mathcal{J}}_{\hat{\xi}} = (\xi_{\hat{\xi}})^2 * \boldsymbol{\mathcal{J}}_\xi^{\mathrm{T}}\boldsymbol{\mathcal{J}}_\xi$ by applying the chain rule, given that $\boldsymbol{\mathcal{J}}_{\hat{\xi}} = \xi_{\hat{\xi}}\boldsymbol{\mathcal{J}}_\xi$. Therefore, $\xi_{\hat{\xi}}$ must be non-zero for all $\hat{\xi}\in\hat{\Omega}$ to ensure a valid transformation of the Jacobian.

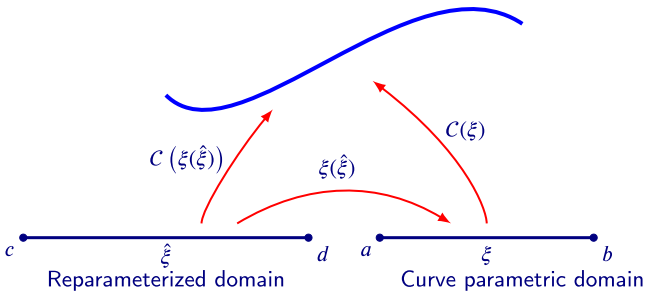

Fig. 24. Schematic illustration of curve reparameterization.

To ensure the curve reparameterization preserves bijectivity, $\xi(\hat{\xi})$ must be a non-decreasing monotonic function. This condition guarantees that $\xi(\hat{\xi})$ remains constant or increases across any interval within its domain. This monotonicity can be verified by examining the first derivative of $\xi(\hat{\xi})$

$$\frac{d\xi}{d\hat{\xi}} = \hat{p} \sum_{i=0}^{m-1} \frac{\beta_i - \beta_{i-1}}{\hat{\xi}_i - \hat{\xi}_{i-1}} N_{i,\hat{p}-1}(\hat{\xi}), \tag{C.8}$$

where $\hat{p}$ is the degree, and $N_{i,\hat{p}-1}(\hat{\xi})$ are the B-spline basis functions of degree $\hat{p}-1$.

Here, we derive the sufficient conditions to ensure the monotonicity of $\xi(\hat{\xi})$. Specifically, the weights associated with successive positions, denoted by β_i, must satisfy the following relationship

$$\beta_i \geq \beta_{i-1}, \ \ i = 1, 2, \ldots, m. \tag{C.9}$$

In other words, the weights in successive positions, β_i, should satisfy $\beta_i \geq \beta_{i-1}$. This constraint ensures that the slope of $\xi(\hat{\xi})$ (i.e., its first derivative) remains non-negative, thereby preserving the monotonicity of $\xi(\hat{\xi})$.

While it would be straightforward to directly incorporate the inequality conditions from Eq. (C.9) into a complex constrained optimization problem, this approach could significantly complicate the solution process. To avoid this complexity, we propose transforming the problem into an equivalent but simpler one with simple bound constraints, where the monotonicity constraints are naturally satisfied.

This simplification is achieved by reformulating the optimization problem in increments θ_i applied to the control coefficients β_i, rather than manipulating the coefficients directly. Consequently, the control points, now expressed through these increments, naturally fulfill the inequality constraints specified in Eq. (C.9). This leads to a streamlined optimization problem with simple bound constraints

$$\begin{cases} \beta_0 = \theta_0 = 0, \\ \beta_i = \beta_{i-1} + \theta_i, \quad \text{for } i = 1, 2, \ldots, m \end{cases} \tag{C.10}$$

where each $\theta_i \geq 0$. This approach ensures that each β_i automatically satisfies the required monotonicity without explicit constraint enforcement in the optimization process.

Finally, we solve the following simple bounded constrained optimization problem

$$\begin{aligned} &\arg\min_{\theta_i} \ \mathcal{E}\left(\theta_i;\ \boldsymbol{C}(\xi(\hat{\xi}))\right)_{\text{ArcLength}} = \frac{1}{L^2} \int_0^1 \left|x'(\xi)\right|^2 d\xi, \\ &\text{s.t.} \quad \theta_i \geq 0. \end{aligned} \tag{C.11}$$

Data availability

Data will be made available on request.

References

[1] A.V. Gusarov, I. Yadroitsev, P. Bertrand, I. Smurov, Model of radiation and heat transfer in laser-powder interaction zone at selective laser melting, J. Heat Transf. 131 (7) (2009) 072101.
[2] M. Bayat, O. Zinovieva, F. Ferrari, C. Ayas, M. Langelaar, J. Spangenberg, R. Salajeghe, K. Poulios, S. Mohanty, O. Sigmund, J. Hattel, Holistic computational design within additive manufacturing through topology optimization combined with multiphysics multi-scale materials and process modelling, Prog. Mater. Sci. 138 (2023) 101129.
[3] B. Schoinochoritis, D. Chantzis, K. Salonitis, Simulation of metallic powder bed additive manufacturing processes with the finite element method: A critical review, Proc. Inst. Mech. Eng. Part B: J. Eng. Manuf. 231 (1) (2017) 96–117.
[4] Z. Luo, Y. Zhao, A survey of finite element analysis of temperature and thermal stress fields in powder bed fusion Additive Manufacturing, Addit. Manuf. 21 (2018) 318–332.
[5] M. Francois, A. Sun, W. King, N. Henson, D. Tourret, C. Bronkhorst, N. Carlson, C. Newman, T. Haut, J. Bakosi, J. Gibbs, V. Livescu, S. Vander Wiel, A. Clarke, M. Schraad, T. Blacker, H. Lim, T. Rodgers, S. Owen, F. Abdeljawad, J. Madison, A. Anderson, J.-L. Fattebert, R. Ferencz, N. Hodge, S. Khairallah, O. Walton, Modeling of additive manufacturing processes for metals: Challenges and opportunities, Curr. Opin. Solid State Mater. Sci. 21 (4) (2017) 198–206.
[6] G. Vastola, G. Zhang, Q. Pei, Y.-W. Zhang, Controlling of residual stress in additive manufacturing of Ti6Al4V by finite element modeling, Addit. Manuf. 12 (2016) 231–239, Special Issue on Modeling & Simulation for Additive Manufacturing.
[7] D. Sarkar, A. Kapil, A. Sharma, Advances in computational modeling for laser powder bed fusion additive manufacturing: A comprehensive review of finite element techniques and strategies, Addit. Manuf. 85 (2024) 104157.
[8] E.R. Denlinger, M. Gouge, J. Irwin, P. Michaleris, Thermomechanical model development and in situ experimental validation of the Laser Powder-Bed Fusion process, Addit. Manuf. 16 (2017) 73–80.
[9] L.-E. Lindgren, Finite element modeling and simulation of welding part 1: increased complexity, J. Therm. Stresses 24 (2) (2001) 141–192.
[10] L.-E. Lindgren, Finite element modeling and simulation of welding. Part 2: improved material modeling, J. Therm. Stresses 24 (3) (2001) 195–231.

[11] L.-E. Lindgren, Finite element modeling and simulation of welding. Part 3: efficiency and integration, J. Therm. Stresses 24 (4) (2001) 305–334.
[12] A. Olleak, Z. Xi, Part-scale finite element modeling of the selective laser melting process with layer-wise adaptive remeshing for thermal history and porosity prediction, J. Manuf. Sci. Eng. 142 (12) (2020) 121006.
[13] I. Roberts, C. Wang, R. Esterlein, M. Stanford, D. Mynors, A three-dimensional finite element analysis of the temperature field during laser melting of metal powders in additive layer manufacturing, Int. J. Mach. Tools Manuf. 49 (12) (2009) 916–923.
[14] X. Lu, X. Lin, M. Chiumenti, M. Cervera, Y. Hu, X. Ji, L. Ma, H. Yang, W. Huang, Residual stress and distortion of rectangular and S-shaped Ti-6Al-4V parts by Directed Energy Deposition: Modelling and experimental calibration, Addit. Manuf. 26 (2019) 166–179.
[15] M. Chiumenti, E. Neiva, E. Salsi, M. Cervera, S. Badia, J. Moya, Z. Chen, C. Lee, C. Davies, Numerical modelling and experimental validation in Selective Laser Melting, Addit. Manuf. 18 (2017) 171–185.
[16] M. Chiumenti, M. Cervera, A. Salmi, C. Agelet de Saracibar, N. Dialami, K. Matsui, Finite element modeling of multi-pass welding and shaped metal deposition processes, Comput. Methods Appl. Mech. Engrg. 199 (37) (2010) 2343–2359.
[17] A. Foroozmehr, M. Badrossamay, E. Foroozmehr, S. Golabi, Finite element simulation of selective laser melting process considering optical penetration depth of laser in powder bed, Mater. Des. 89 (2016) 255–263.
[18] M. Gouge, E. Denlinger, J. Irwin, C. Li, P. Michaleris, Experimental validation of thermo-mechanical part-scale modeling for laser powder bed fusion processes, Addit. Manuf. 29 (2019) 100771.
[19] S. Kollmannsberger, A. Özcan, M. Carraturo, N. Zander, E. Rank, A hierarchical computational model for moving thermal loads and phase changes with applications to selective laser melting, Comput. Math. Appl. 75 (5) (2018) 1483–1497.
[20] J.P. Leonor, G.J. Wagner, GO-MELT: GPU-optimized multilevel execution of LPBF thermal simulations, Comput. Methods Appl. Mech. Engrg. 426 (2024) 116977.
[21] P. Kopp, E. Rank, V.M. Calo, S. Kollmannsberger, Efficient multi-level hp-finite elements in arbitrary dimensions, Comput. Methods Appl. Mech. Engrg. 401 (2022) 115575.
[22] C.A. Moreira, M.A. Caicedo, M. Cervera, M. Chiumenti, J. Baiges, A multi-criteria h-adaptive finite-element framework for industrial part-scale thermal analysis in additive manufacturing processes, Eng. Comput. 38 (6) (2022) 4791–4813.
[23] C. Li, E.R. Denlinger, M.F. Gouge, J.E. Irwin, P. Michaleris, Numerical verification of an octree mesh coarsening strategy for simulating additive manufacturing processes, Addit. Manuf. 30 (2019) 100903.
[24] A. Olleak, Z. Xi, Scan-wise adaptive remeshing for efficient LPBF process simulation: The thermal problem, Manuf. Lett. 23 (2020) 75–78.
[25] A. Olleak, F. Dugast, P. Bharadwaj, S. Strayer, S. Hinnebusch, S. Narra, A.C. To, Enabling Part-Scale Scanwise process simulation for predicting melt pool variation in LPBF by combining GPU-based Matrix-free FEM and adaptive remeshing, Addit. Manuf. Lett. 3 (2022) 100051.
[26] Y. Yang, M. Knol, F. van Keulen, C. Ayas, A semi-analytical thermal modelling approach for selective laser melting, Addit. Manuf. 21 (2018) 284–297.
[27] J. Ning, E. Mirkoohi, Y. Dong, D.E. Sievers, H. Garmestani, S.Y. Liang, Analytical modeling of 3D temperature distribution in selective laser melting of Ti-6Al-4V considering part boundary conditions, J. Manuf. Process. 44 (2019) 319–326.
[28] Y. Yang, M. Knol, F. van Keulen, C. Ayas, A semi-analytical thermal modelling approach for selective laser melting, Addit. Manuf. 21 (2018) 284–297.
[29] J.C. Steuben, A.J. Birnbaum, J.G. Michopoulos, A.P. Iliopoulos, Enriched analytical solutions for additive manufacturing modeling and simulation, Addit. Manuf. 25 (2019) 437–447.
[30] A.J. Wolfer, J. Aires, K. Wheeler, J.-P. Delplanque, A. Rubenchik, A. Anderson, S. Khairallah, Fast solution strategy for transient heat conduction for arbitrary scan paths in additive manufacturing, Addit. Manuf. 30 (2019) 100898.
[31] E.J. Schwalbach, S.P. Donegan, M.G. Chapman, K.J. Chaput, M.A. Groeber, A discrete source model of powder bed fusion additive manufacturing thermal history, Addit. Manuf. 25 (2019) 485–498.
[32] Y. Wang, X. Ji, S.Y. Liang, Analytical modeling of temperature distribution in laser powder bed fusion with different scan strategies, Opt. Laser Technol. 157 (2023) 108708.
[33] P.R. Zagade, B. Gautham, A. De, T. DebRoy, Analytical modelling of scanning strategy effect on temperature field and melt track dimensions in laser powder bed fusion, Addit. Manuf. 82 (2024) 104046.
[34] A. Plotkowski, M.M. Kirka, S. Babu, Verification and validation of a rapid heat transfer calculation methodology for transient melt pool solidification conditions in powder bed metal additive manufacturing, Addit. Manuf. 18 (2017) 256–268.
[35] A. Ross, I. Bitharas, K. Perkins, A. Moore, Volumetric heat source calibration for laser powder bed fusion, Addit. Manuf. 60 (2022) 103267.
[36] Y. Jia, Y. Saadlaoui, J.-C. Roux, J.-M. Bergheau, Steady-state thermal model based on new dedicated boundary conditions–application in the simulation of laser powder bed fusion process, Appl. Math. Model. 112 (2022) 749–766.
[37] R. Forslund, A. Snis, S. Larsson, Analytical solution for heat conduction due to a moving Gaussian heat flux with piecewise constant parameters, Appl. Math. Model. 66 (2019) 227–240.
[38] B. Stump, A. Plotkowski, An adaptive integration scheme for heat conduction in additive manufacturing, Appl. Math. Model. 75 (2019) 787–805.
[39] T. Moran, D. Warner, N. Phan, Scan-by-scan part-scale thermal modelling for defect prediction in metal additive manufacturing, Addit. Manuf. 37 (2021) 101667.
[40] A. Robert, T. Debroy, Geometry of laser spot welds from dimensionless numbers, Met. Mater. Trans. B 32 (2001) 941–947.
[41] D. Veldman, R. Fey, H. Zwart, M. van de Wal, J. van den Boom, H. Nijmeijer, Semi-analytic approximation of the temperature field resulting from moving heat loads, Int. J. Heat Mass Transfer 122 (2018) 128–137.
[42] H.S. Carslaw, J.C. Jaeger, Conduction of Heat in Solids, Oxford Science Publications, Clarendon Press, 1986.
[43] L. Piegl, W. Tiller, The NURBS book, Springer Science & Business Media, 2012.
[44] Y. Cao, X. Lin, N. Kang, L. Ma, L. Wei, M. Zheng, J. Yu, D. Peng, W. Huang, A novel high-efficient finite element analysis method of powder bed fusion additive manufacturing, Addit. Manuf. 46 (2021) 102187.
[45] M. Vanini, S. Searle, K. Vanmeensel, B. Vrancken, Avoiding heat source calibration for finite element modeling of the laser powder bed fusion process, Addit. Manuf. 92 (2024) 104369.
[46] Z.-D. Zhang, S. Imani Shahabad, O. Ibhadode, C.F. Dibia, A. Bonakdar, E. Toyserkani, 3-dimensional heat transfer modeling for laser powder bed fusion additive manufacturing using parallel computing and adaptive mesh, Opt. Laser Technol. 158 (2023) 108839.
[47] B.A. Boley, J.H. Weiner, Theory of Thermal Stresses, John Wiley & Sons, 1960.
[48] T. Bar-Kohany, A. Jain, Dissipation of boundary effects in multilayer heat conduction problems, Int. J. Heat Mass Transfer 223 (2024) 125207.
[49] R.T. Farouki, T. Sakkalis, Real rational curves are not ‘unit speed’, Comput. Aided Geom. Design 8 (2) (1991) 151–157.